1 Synoptic Ozone, Cloud Reflectivity, and Erythemal Irradiance from Sunrise to Sunset for the Whole Earth
2   as viewed by the DSCOVR spacecraft from the Earth Sun Lagrange-1 Orbit

3 Jay Herman[1], Liang Huang[2], Richard McPeters[3], Jerry Ziemke[3], Alexander Cede[4], Karin Blank[3]

4 Abstract

5 EPIC (Earth Polychromatic Imaging Camera) onboard the DSCOVR (Deep Space Climate Observatory)
6 spacecraft is the first Earth science instrument located near the Earth-Sun gravitational plus centrifugal
7 force balance point, Lagrange-1. EPIC measures Earth reflected radiances in 10 wavelength channels
8 ranging from 317.5 nm to 779.5 nm. Of these channels, four are in the UV range 317.5, 325, 340, and
9 388 nm, which are used to retrieve O_3, 388 nm scene reflectivity (LER Lambert Equivalent Reflectivity),
10 SO_2, and aerosol properties. Unlike low earth orbiting satellite instruments, these quantities are derived
11 synoptically at Goddard Space Flight Center for the entire sunlit globe from sunrise to sunset every 68
12 minutes when it is summer or 110 minutes in winter at the receiving antenna in Wallops Island, Virginia,
13 respectively. Depending on solar zenith angle, either 317.5 or 325 nm channels are combined with 340
14 and 388 nm to derive ozone amounts. As part of the ozone algorithm, the 388 nm channel is used to
15 derive LER.   The retrieved ozone amounts and LER are combined to derive the Erythemal irradiance for
16 the entire sunlit Earth's surface, 2048x2048 points, at a nadir resolution of 18 x 18 km^2 using a
17 computationally efficient approximation to a radiative transfer calculation of irradiance. Corrections are
18 made for altitude above sea level and for the reduced transmission by clouds based on retrieved LER.

22 [1]University of Maryland Baltimore County, Maryland

23 [2]Science Systems and Applications, Lanham, Maryland

24 [3]NASA Goddard Space Flight Center, Greenbelt, Maryland

25 [4]SciGlob Instruments and Services, Maryland

28 DSCOVR/EPIC Synoptic Ozone, Cloud Reflectivity, and Erythemal Irradiance From Sunrise to Sunset for
29 the Whole Earth as viewed from an Earth-Sun Lagrange-1 Orbit

30 **1.0 Introduction**

31 The DSCOVR (Deep Space Climate Observatory) spacecraft was successfully launched on 11
32 February 2015 to an orbit near the Earth-Sun gravitational plus centrifugal force balance point,
33 Lagrange-1 (L-1), 1.5×10^6 km from the Earth. The earth pointing instruments on the DSCOVR spacecraft
34 placed in orbit about the L-1 point will simultaneously observe the sun illuminated earth's disk from
35 sunrise to sunset. An illustration of the orbit is given in the Appendix (see https://epic.gsfc.nasa.gov for
36 details). DSCOVR started to transmit Earth data after it achieved a quasi-stable orbit in mid-June 2015.
37 The DSCOVR mission at L-1 is optimum for early warning solar flare observations (magnetic field,
38 electron, and proton fluxes) from instruments contained on the sunward side of DSCOVR, and contains
39 two Earth-viewing instruments allowing continuous observation of the sunlit face of the Earth. The EPIC
40 (Earth Polychromatic Imaging Camera) instrument onboard DSCOVR images the Earth in ten narrow
41 band wavelength channels (up to 2048 x 2048 pixels), producing both color images of the Earth and
42 science data products such as ozone, SO_2, aerosol amounts, cloud reflectivity, UV surface irradiance,
43 cloud and aerosol heights, and vegetation indices. This paper discusses the UV science products O_3,
44 cloud reflectivity, and UV surface irradiance, methods of retrieval, and EPIC's UV in-flight calibration.

45 The data and images of the changing synoptic cloud cover from sunrise to sunset are unique to
46 the EPIC satellite instrument. Neither geostationary nor low earth orbiting satellites can produce these
47 data or images. Geostationary satellites could produce something similar, but to date, none have the UV
48 channels for ozone and LER, and geostationary satellites are limited to a range of approximately $\pm 60^O$
49 latitude and $\pm 60^O$ longitude. While low earth orbiting satellite data can be combined to produce a global
50 representation of ozone and cloud cover, all the ozone and cloud cover are for a fixed local time (e.g.,
51 13:30 hours for OMI) and is not representative of the atmosphere at other times of the day.

52 **1.1 EPIC Instrument**

53 The EPIC instrument consists of a 30-cm aperture 283.642 cm focal length Cassegrain telescope
54 containing a multi-element field-lens group focusing light onto a UV sensitive 2048 x 2048 hafnium
55 coated CCD detector with 12 bit readout electronics. Images are made through ten narrow-band filters,
56 four in the ultraviolet, four in the visible, and two in the near infrared. The 10 filter transmission
57 functions are shown in Fig. 1. Observations are made as light passes sequentially through each of ten
58 narrow-band filters mounted in two moveable filter wheels and through an exposure control 3-slot
59 rotating shutter. The exposure times for each wavelength were adjusted in-flight to achieve an
60 approximately 80 % CCD electron well fill in the brightest scenes, which were observed during the first
61 week of operation, to avoid saturation and leaking from one pixel to another (blooming). Earth exposure
62 times range from about 654 milliseconds at 317.5 nm to 22 milliseconds at 551 nm, which have not
63 changed during the current life of the mission. Another set of exposure times was determined for
64 viewing the full moon as seen from the Earth (Table 1). The CCD has a well depth of approximately
65 8.5×10^4 electrons (a maximum signal to noise ratio SNR of 290:1) before a small dark current correction
66 that is a function of its in-flight operating temperature of -20^OC. The 12-bit readout means that there

67   are 2^{11} (2048) readout steps or counts (42 electrons/count). The counts divided by the exposure time

68   (counts/second) are converted to radiances or albedos using in-flight scene matching calibration from

69   low earth orbit satellites (see Sect. 1.2 and Table 2). The maximum SNR applies to the brightest of

70   scenes over high clouds or fresh snow over ice. Cloud-free and snow-free scenes have much lower SNR,

71   which affects the visible channels more than the UV channels because of the lower scene contrasts with

72   clouds caused by enhanced UV Rayleigh scattering. There are occasional bright flashes caused by ice

73   crystals in high clouds that saturate a few pixels (see Fig. 2 and Marshak et al., 2017) in the equatorial

74   and mid-latitude regions.

75   The filters of interest for calculating ozone amounts, aerosol index, and cloud reflectivity are

76   centered on 317.5, 325, 340, and 388 nm in the wavelength band with full widths at half maximum

77   (FWHMs) 1.0, 1.0, 2.7, and 2.6 nm, respectively. For the UV channels, 2 x 2 individual pixels are

78   averaged onboard the spacecraft to yield an effective 1024 x 1024 pixel image corresponding to an 18 x

79   18 km^2 resolution at the observed center of the Earth's sunlit disk. The effective spatial resolution

80   decreases as the secant of the angle between EPIC's sub-earth point and the normal to the earth's

81   surface. Only the 443 nm channel is retrieved at full resolution to help with resolving cloud cover and

82   obtaining improved color images. The sampling resolution of a single pixel is about 8 x 8 km^2 (about 1

83   arcsecond), but including the effect of the optical point-spread function, the effective 443 nm channel

84   resolution is about 10 km. The effective resolution at 443 nm has been verified by looking at clear

85   scenes over the Nile River in Egypt and, occasionally, the cloud-free Amazon River in Brazil.

86

87   EPIC data has been obtained since June 15, 2015 at a rate of one set of 10 wavelengths every 68

88   minutes during Northern Hemisphere (NH) summer and one set every 110 minutes in the winter. The

89   difference between summer and winter rates is caused by the reduced number of hours in the winter

90   when the antenna (located at Wallops Island, Virginia) is in view of the spacecraft, and limitations from

91   the spacecraft memory technology from the late 1990s.

92

93   Each of the 10-wavelength measurements is obtained at slightly different times. The first filter in

94   the sequence is 443 nm, which takes about 2 minutes to complete a measurement (28 ms exposure

95   time (Table 1) plus CCD readout and onboard processing time that includes 12-bit jpeg compression of a

96   2048 x 2048 pixel image). The remaining 9 filter measurements take a total of about 5 minutes

97   (exposure times plus CCD readout into memory) and then another 13 minutes to process the data for

98   the 9 filters (this includes 12-bit jpeg compression of 1024 x 1024 images that have been averaged

99   onboard in groups of 2x2 pixels before compression). Adjacent pairs of wavelengths are measured at 30

100   second intervals before the onboard processing is started. This means the individual channel images are

101   not co-located at the pixel level because of earth rotation (15.03^O per hour or about 1670 km per hour

102   at the equator), the slow rotation of the spacecraft, 0.082^O per hour, and a small amount of spacecraft

103   jitter). Each pixel views about 1 arc second or 2.78×10^{-4} degrees. Data from an onboard star-tracker and

104   feedback from the earth's image on the CCD keep the images approximately centered on the CCD. The

105   lack of native channel-to-channel colocation requires an elaborate spherical geometry geolocation

106   analysis to adjust the data to a common latitude x longitude grid with an accuracy of 1/4 of a pixel.

107   A description of the EPIC instrument, its orbit, and some of the data products can be obtained
108   from http://avdc.gsfc.nasa.gov/pub/DSCOVR/Web_EPIC/ and from http://epic.gsfc.nasa.gov/. The EPIC
109   raw counts/second and science data (Version 2 used in this paper) are archived at
110   https://eosweb.larc.nasa.gov/project/dscovr/dscovr_table in HDF5 format.
111
112   This paper presents examples of the ozone and scene reflectivity retrievals that are used to
113   obtain unique estimates of erythemal UV irradiance (or UV Index, UVI) as a function of latitude,
114   longitude, local solar time (LST), and altitude above sea level (ASL). Since this is the first paper on EPIC
115   retrieved ozone, Sect. 1 contains a brief description of the calibration of the four UV channels and the
116   ozone retrieval algorithm. Sect. 2 shows examples of natural color images, Sect. 3 gives an example of
117   retrieved ozone and the corresponding 388 nm Lambert Equivalent Reflectivity (LER, Herman et al.,
118   2009), Sect. 4 presents a validation of EPIC retrieved ozone compared to ozone from ground-based and
119   satellite data, Sect. 5 shows details of the latitudinal and longitudinal synoptic variability of ozone, and
120   Sect. 6 presents new results showing the sunrise to sunset variability of UV erythemal radiation reaching
121   the Earth's surface including the reduction by clouds from sunrise to sunset.

122   **1.2 Calibration**

123   Before the raw EPIC data (counts per second) can be used, a number of pre-processing steps
124   must be accomplished. The major steps are 1) measuring and subtracting the dark current signal, 2)
125   "flat-fielding" the CCD so that the sensitivity differences between all four million pixels are determined
126   and corrected, 3) correcting for stray-light effects to account for light that should be going to a particular
127   pixel, but instead is scattered to different pixels, and 4) determining the radiometric calibration for each
128   wavelength channel in terms of EPIC counts/second to be converted to earth normalized radiances or
129   reflectances (backscattered at approximately 172°). The earth upwelling normalized radiance I_M (W/(m^2
130   nm sr)) at the top of the atmosphere (TOA) is defined in terms of the albedo A_M given by Eq. 1,

$$A_M = \frac{I_M}{S_M/D_E^2} \quad (\text{sr}^{-1})$$

(1)

131   for wavelength bands M=1 to 4, S_M is the incident solar irradiance (W/(m^2 nm)) weighted with the filter
132   function for band M at 1 AU and D_E is the sun-earth distance in AU (astronomical units). Since EPIC does
133   not measure solar irradiance, we use a high resolution solar irradiance spectrum, S(λ) (Dobber et al.,
134   2008), as a reference solar spectrum. The reference spectrum is weighted with EPIC's filter transmission
135   functions T_M(λ) (Fig. 1) to obtain each EPIC channel's weighted solar irradiance S_M at solar-earth
136   distance at 1 astronomical unit (Eqs. 1 and 2).

$$S_M = \int_{\lambda_1}^{\lambda_2} T_M(\lambda)S(\lambda)d\lambda \Big/ \int_{\lambda_1}^{\lambda_2} T_M(\lambda)d\lambda \quad (\text{Wm}^{-2}\text{nm}^{-1})$$

(2)

137

138   In-flight radiometric calibration is accomplished by comparison with albedo values measured by
139   current well-calibrated LEO (low-earth orbiting; e.g., Aura/OMI, Ozone Monitoring Instrument, and
140   Suomi-NPP/OMPS, National Polar-orbiting Partnership/Ozone Mapping and Profiler Suite) satellite
141   instruments observing scenes that match in time and observing angles with those from EPIC. For albedo
142   measurements, OMPS has a calibration accuracy of 2 %, while its wavelength dependence (precision) in
143   the calibration is estimated to be better than 1 % (Jaross et al., 2014). The OMPS Nadir Mapper on
144   Suomi-NPP has a 50 x 50 km^2 footprint in its normal operating mode with 36 cross-track views ($\pm55^o$
145   satellite view angle or strip of about $\pm12^O$ equatorial longitude). It has a spectral resolution of 1 nm,
146   which is close to EPIC's 317.5 nm and 325 nm channels FWHM, but narrower than EPIC's 340 nm and
147   388 nm channels. To perform in-flight calibration, OMPS' albedo spectra were either interpolated (for
148   317.5 and 325 nm channels) or convolved (at 340 and 388 nm) with each EPIC filter transmission
149   function T_M (Fig. 1). Because the albedo spectra $A_M(\lambda)$ (Eq. 1) removes the Fraunhofer line structure
150   contained in both the solar irradiance S_M and the reflected Earth radiance $I_M(\lambda)$, the interpolation and
151   convolution of $A_M(\lambda)$ has better accuracy than directly using $I_M(\lambda)$. OMI on Aura has 13 x 24 km^2 spatial
152   resolution and about $\pm56^o$ cross-track views (a strip of $\pm$ 1300 km or $\pm$ 13° equatorial longitude) with a
153   spectral resolution of 0.42 nm. To match measurements with DSCOVR, OMI's albedo spectra were
154   convolved with EPIC's $T_M(\lambda)$. Then, the results in every two adjacent cross-track views and four
155   consecutive along-track scans are combined to form 50 x 50 km^2 footprints for comparison with EPIC
156   measured counts/second obtained from 7 x 7 EPIC pixels.

157   EPIC raw counts/second inside each coincident footprint are preprocessed by the steps stated in
158   a previous paragraph. Then, the counts/second average and variance in each coincident footprint are
159   computed to obtain the EPIC albedo calibration coefficients K_M (Eq. 3). Misalignment between EPIC and
160   OMPS or OMI footprints can result large scene noise unless uniform scenes are selected and less
161   uniform scenes discarded. This is achieved by weighting each coincident data point with the reciprocal
162   of the percent EPIC counts/second variance inside the coincident footprint. All of the coincident points
163   between LEO satellites and EPIC observations occur within $\pm40^o$ of the earth's equator. Selected LEO
164   footprints have viewing angles nearly identical to EPIC's (within 1° in backscatter angle and 2° degrees in
165   solar zenith angle).   EPIC's backscatter angle varies with latitude and longitude by less than 0.25^o, since
166   the angular size of the earth varies from 0.45^O to 0.53^O to 0.45^O every 6 months depending on the
167   location of DSCOVR in its orbit (an irregular Lissajous orbit about L-1 that is tilted relative to the ecliptic
168   plane and perturbed by the Earth's moon). The orbit varies from 4° to 15° away from the Earth-Sun line.
169   These small differences in observing geometry are corrected in the atmospheric radiative transfer model
170   calculations $\alpha(\lambda)$ (Eq. 4), resulting in corrections less than 2 %. EPIC albedo calibration coefficients are
171   derived from Eqs. 3 and 4.

$$K_M = \frac{A_M(OMPS)\{\alpha_M(EPIC)/\alpha_M(OMPS)\}}{C_M(EPIC)D_E^2} \qquad (3)$$

$$\alpha_M = \int \alpha(\lambda)S(\lambda)T_M(\lambda)\,d\lambda \bigg/ \int S(\lambda)T_M(\lambda)\,d\lambda \qquad (4)$$

172

173   where

174   M is the EPIC channel number, M=1,2,3,4
175    $A_M(OMPS)$ = OMPS albedo measurement in the EPIC channel-M wavelength band
176    $\alpha_M(EPIC)$ and $\alpha_M(OMPS)$ are computed albedo values for EPIC and OMPS coincident geometry,
177    $C_M(EPIC)$ is the average count rate over the pixels matching OMPS,
178   D_E is the sun-earth distance in AU.
179    $\alpha(\lambda)$ is the computed high resolution normalized radiance spectrum,
180    $S(\lambda)$ is the referenced high resolution solar irradiance spectrum,
181    $T_M(\lambda)$ is the EPIC filter transmission profile or the OMPS slit function.

182
183   All of the coincidence points with LEO satellite instruments were measured using the area of
184   the EPIC CCD within 600 pixels of its center. There are about 15000 coincidence data points accumulated
185   by the end of 2016. Because of the large number of data points, statistical averaging errors are small.
186   An atmospheric radiative transfer model, RTM, takes total column ozone and surface reflectivity from
187   LEO retrievals to obtain both $\alpha_M(EPIC)$ and $\alpha_M(LEO)$. Although uncertainties in the RTM can propagate
188   into the computed albedos, the resulting uncertainties in $\alpha_M(EPIC)$ and $\alpha_M(LEO)$ are approximately
189   identical, and approximately cancel in Eq. 3. The resulting EPIC albedo calibration uncertainty is mostly
190   inherited from the OMPS albedo calibration uncertainty, which has an accuracy of 2 % and a precision of
191   1 % in relative (wavelength dependent) values. For the UV channels, the calibration factors K_M are not
192   constants, but are slowly increasing functions of time (on average 0.016 per year; see $K_M(t)$ in Fig. 2),
193   which is normalized to one on 1 January 2016). Table 2 shows the reference values of K_M multiplied by
194   π.

195   Using Tables 1, 2, and Fig. 2, EPIC albedo measurements are derived with
196

$$A_M(EPIC) = K_M C_M(EPIC) D_E^2 \qquad\qquad (1\text{-}5)$$

197
198

199   Note that the factor D_E^2 for solar irradiance at 1 AU is contained in the albedo calibration
200   coefficient K_M. Since solar activity changes (e.g., 27.5 day cycle) are negligible for EPIC UV channel
201   wavelengths, daily solar irradiance changes are only adjusted with the sun-earth distance D_E. Users of
202   EPIC data may also be interested in radiance measurements. The radiance calibration coefficients can
203   be derived with Eq. 6,
204

$$E_M = K_M S_M \qquad\qquad (6)$$

205
206
207   and the radiance measurements can be obtained with Eq. 7.
208

$$I_M(EPIC) = E_M C_M(EPIC) \qquad\qquad (7)$$

209
210

211   The uncertainty in the radiance calibration can increase significantly due to errors in estimating
212 the absolute solar irradiance. Uncertainty in estimated S_M for EPIC UV channels in Table 1 is about 3 %.

213   **1.3 Ozone Algorithm**

214

215   Once the albedo calibration factors are applied to EPIC's measured counts/second, the
216 calculated albedos can be combined to retrieve total column ozone (TCO), Lambert Equivalent
217 Reflectivity (LER), and aerosol index (AI). The TOA directional albedo calculation uses the TOMRAD
218 radiative transfer calculation code, which has a spherical geometry correction for large solar zenith
219 angles (SZA) and satellite looking angles (SLA) (Caudill et al., 1997). The calculation uses the same
220 climatological ozone profiles used in OMI retrievals, altitude weighted average effective ozone
221 temperatures, ground reflectivities, terrain height, and climatological cloud heights. Spectrally resolved
222 O_3 absorption cross sections are from Brion et al., (1993, 1998); Daumont et al., (1992); and Malicet et
223 al., (1995). The resulting spectra are convolved with the EPIC filter transmission functions (Fig. 1) and
224 with the reference solar irradiance spectra (see Eq. 4).

225

226   The resulting computed α_M (Eq. 4) are compiled into a finely stepped look-up table as functions
227 of ozone profiles and solar-view angles.   EPIC ozone retrieval uses the 388 nm channel for computing
228 the surface reflectivity with a formula similar (except for choice of wavelengths) to that used in cloud
229 reflectivity studies (Herman et al., 2009). Then, the retrieval is based on two ozone absorption channels,
230 317.5 nm and 340 nm for low optical depth conditions, or 325 nm and 340 nm for high optical depth
231 conditions, together with the 388 nm measurement to form triplet equations. The ozone retrieval
232 algorithm assumes a linear wavelength dependence in the surface reflectivity (Eq. 8),

$$R_\lambda = R_{\lambda_0} + b(\lambda - \lambda_0) \qquad (8)$$

233

234 where λ_0 is given wavelength 388 nm. The total column ozone (TCO) is given by Eq. 9,

$$\Omega = \Omega_0 + \frac{\Delta N_{\lambda_1} \frac{\partial N_{\lambda_2}}{\partial R}(\lambda_2 - \lambda_0) - \Delta N_{\lambda_2}\frac{\partial N_{\lambda_1}}{\partial R}(\lambda_1 - \lambda_0)}{\frac{\partial N_{\lambda_1}}{\partial \Omega}\frac{\partial N_{\lambda_2}}{\partial R}(\lambda_2 - \lambda_0) - \frac{\partial N_{\lambda_2}}{\partial \Omega}\frac{\partial N_{\lambda_1}}{\partial R}(\lambda_1 - \lambda_0)} \qquad (9)$$

235 where

236 Ω_0 is an initial climatology estimate of TCO or TCO from previous step in the iteration,
237 λ_1 and λ_2 are the selected ozone absorption wavelengths,
238 N_λ is the N-value defined as logarithm of the albedo values by Eq. 10,
239

$$N_\lambda = -100\, log_{10}\{I_\lambda/(S_\lambda/D^2)\} \qquad (10)$$

240

241 and

242 ΔN_λ is the N-value residue (difference between the measured N-value and the computed N-value),

243     $\dfrac{\partial N_{\lambda_x}}{\partial Z}$ = measurement sensitivity with respect to the total column ozone, Z = Ω, or the surface

244   reflectivity, Z = R, for wavelengths λ_1 or λ_2.

245   If one assumes the sensitivities to the surface reflectivity, ∂N$_\lambda$/∂R are wavelength independent,

246   Eq. 5 for the triplet algorithm is similar to the Version 8 TOMS algorithm (Rodriguez et al., 2003).

247   Since the algorithm for ozone (Eqs. 8 to 10) requires the use of two or more wavelength

248   channels, the measured counts/second for each channel must be geolocated on a common latitude x

249   longitude grid that is accurate to 0.25 of a single pixel size. When projected on the 3-D Earth, the

250   sampling size is about 8 km at nadir and effectively increases to 10 km when EPIC's point spread

251   function is applied. The result for 2 x 2 pixel averaging is a spatial resolution at nadir of about 18 km,

252   which gets larger as the secant of the SLA from the nadir point. SLA is measured relative to the normal

253   to the Earth's surface, and is 0° at nadir and almost 90° at the Earth's sunlit terminator. The radiative

254   transfer spherical geometry correction is accurate to about 80° in SZA and SLA, which means that

255   retrieved ozone values near the Earth's terminator are not accurate.

256   **2   Natural Color Images**

257   A typical eye response color image view of the Earth, obtained by a weighted combination of

258   the geolocated red, green, and blue wavelength channels, is shown in Fig. 2. To produce RGB images

259   adjusted to the human eye response, the algorithm used is a derivative of the International Commission

260   on Illumination (CIE) process for estimating tristimulous values from calibrated instruments (Wyszecki

261   and Stiles, 1982; Broadbent, 2004; Gardner, 2007; Bodrogi and Khanh, 2012). Obtaining eye response

262   images for EPIC's narrow band filters (Table 1) was improved by customization of the algorithm to use

263   additional channels than just the 443, 551, and 680 nm blue, green, and red channels.

264   Because the blue 443 nm channel is not spatially averaged onboard the spacecraft, the color

265   images have a maximum resolution of about 10 km at nadir determined by looking at the discernable

266   width of the Nile and Amazon Rivers. The color images also give an indication of the quality of the

267   geolocation. Errors in geolocation would appear as pink edges at the cloud boundaries, which are not

268   present in the images in Figs. 3 or in the complete image collection on http://epic.gsfc.nasa.gov/.

269   Even with accurate geolocation, about 0.25 pixels (2 km), between the 4 UV channels, there is

270   some noise introduced into ozone retrievals by small cloud edge location errors when transferring all of

271   the native data to a common latitude and longitude grid. Ozone retrievals over almost cloud-free

272   scenes, such as over the Saharan desert or clear-sky portions of the oceans, show much less noise than

273   those with partial cloud cover. Since the pixel-to-pixel noise caused by misaligned cloud edges is almost

274   random, spatial averaging to about 50x50 km^2 (similar to TOMS and OMPS, but coarser than OMI spatial

275   resolution) reduces the effect of apparent noise from cloud edges. The following sections use 25 x 25

276   km^2 spatial averaging (3 x 3 CCD pixels), which has more spatial details and some cloud-edge noise

277   (noise < 3 %).

278

3 Examples of EPIC Ozone and Reflectivity

A matched pair of images for ozone and scene reflectivity LER (17 April 2016) are shown in Fig. 4 with a maximum resolution of 18 km, since all UV channels involved in the ozone retrieval are downlinked from the spacecraft at a resolution of 2 x 2 onboard averaged pixels. Note that the reduced resolution hdf5 data files stored on the ground are in their original sampling density (2048 x 2048), but have reduced spatial resolution. In Fig. 4, the entire data image for ozone and the LER scene reflectivity are all at a common Universal Time (00:36 UTC or 12:36 local time at the center of the image) and encompasses local times from sunrise (west) to sunset (east) with all images rotated so that north is up. In the LER scene, a large east-west belt of clouds are visible near the equator, as are cloud plumes descending from the Arctic. The major cloud patterns change slowly, but show major seasonal changes. Figure 5 shows six additional scenes from the same day, 17 April 2016, with large cloud features associated with the Arctic region, an equatorial cloud band, and large cloud structures over the Antarctic Ocean. Figure 6 shows reflectivity measurements for 23 November 2015 with cloud features common in the Southern Hemisphere SH. The cloud band extending toward the Antarctic region from Argentina's Salado River is an example of a persistent feature that appears frequently throughout the year. In a later section, the amounts of retrieved ozone and cloud reflectivity $0 < R_C < 1$ are used to estimate the amount of UV radiation reaching the earth's surface over snow/ice free scenes.

The Arctic and Antarctic ice sheets are visible after their spring equinox times, and especially in their respective late spring and summer images when the Earth's poles are tilted toward L-1 (Figs. 5 and 6). In the color and LER images, clouds over ice are not readily visible because of the very high ice reflectivity providing little or no contrast with 388 nm cloud reflectivity. It is possible to obtain information about clouds over ice from the O_2 A-band channel at 764 nm (Fig. 7), which differentiates between reflecting surfaces that are at different altitudes because of oxygen absorption in the atmosphere. In this image, the bright white clouds (less atmospheric O_2 absorption) are at higher altitudes than the grey clouds, which are all higher than the ice surfaces. A quantitative analysis of cloud height and cloud-caused reduction in solar irradiance reaching the ice surface will be the subject of a future paper.

4 Validation of EPIC Ozone Retrieval

EPIC retrieved ozone can be validated by comparison with other ozone measuring satellite data (e.g., OMI, and OMPS) and by comparison with well-calibrated ground-based instruments.

While EPIC observes from sunrise to sunset in every image, there are only 6 to 8 useful coincidences per 24 hours with a specified ground site separated by either 68 minutes (NH summer) or 110 minutes (NH winter). Coincidences at high SZA > 75° are increasingly inaccurate for both satellite and ground-based retrievals. This problem is compounded for EPIC, since high SZA also implies high SLA, which increases the spherical geometry correction error. Ozone absorption and Rayleigh scattering at high SZA also prevents 317.5 nm radiances from reaching into the lower troposphere and to the surface, which is partially mitigated by having the retrieval algorithm automatically switch from 317.5 nm to 325 nm at high optical depths (usually high SZA).

A comparison of EPIC retrieved TCO with those determined by a Pandora spectrometer instrument (#034) located at Boulder, Colorado is shown in Fig. 8. This Pandora was selected because it has been extensively compared to a well calibrated Dobson spectroradiometer and to OMI and OMPS ozone overpass data (Herman et al., 2015). The Pandora data are matched in location and time t_O to the EPIC UTC when Boulder, Colorado is in view (several times per 24 hours). Pandora ozone is averaged over t_O ±12 minutes. EPIC data are limited to distances within 50 km of Boulder, Colorado. Figure 8 shows that EPIC and Pandora ozone amounts track each other closely during 2015 and 2016. The 2015-2016 average agreement is 2.7 ± 4.9 %. There is a period in the winter of 2016 where the Pandora data quality was degraded by the presence of heavy cloud cover and in February by a mechanical problem with the Pandora sun tracker.

The OMI and OMPS satellites are polar orbiting with an equator crossing time of about 13:30 hours local time measuring in a narrow strip on either side of the orbital track. While it is possible to compare EPIC ozone with low earth orbit satellite data, a more complete comparison can be made with the assimilated ozone product from MERRA-2, the Modern-Era Retrospective Analysis for Research and Applications, (Rotman et al., 2002) version 2 (MERRA-2, Molod et al., 2014). MERRA-2 ozone is based on Microwave Limb Sounder (MLS) and total column ozone from the Ozone Monitoring Instrument OMI on NASA's EOS *Aura* satellite. The advantage of using MERRA-2 is that the ozone field is synoptic and can be directly compared with EPIC for the same UTC (Fig. 9) over the same sunlit globe as seen by EPIC. The ozone structures seen by EPIC are all present in the MERRA-2 independent assimilation, even though there is an average offset of about 10 DU (3 %). The disagreement with EPIC is similar to the offset of MERRA-2 with other satellite data (Wargan et al., 2017). A close look at the ozone maps in Fig. 9 shows overall agreement with most features including the small region of elevated O_3 over the central US. There are differences, such as the higher amount of O_3 measured by EPIC over Brazil on 23 November and the structure at 15^ON in the transition from equatorial O_3 values to mid-latitude values (dark blue to light blue).

5.0 Synoptic Variation of Ozone (SVO) from Sunrise to Sunset

Most LEO satellite views of ozone are at almost fixed local time based on the equator crossing local solar time (13.5 ± 0.8 hours side scanning) with approximately 20 minutes local time variation from the equator to the pole. Longitudinal coverage is obtained by piecing together North-South strips obtained about 90 minutes apart. Variation that occurs on a scale less than 90 minutes cannot be seen from a polar orbiting LEO satellite, nor can variation from different local times of the day. EPIC observes from close to sunrise and sunset with local solar noon near the center of the data set as shown in Fig. 10. The exact position of noon in the EPIC images depends on the location of EPIC in its orbit relative to the Earth-Sun line. The longitude resolution is approximately 0.25^O at the center of the FOV, which corresponds to a time resolution of about 1 minute. The resolution decreases as the secant of the angle from the center (e.g., 2 minutes or 0.5^O at 60° from the center). A limitation in the EPIC observations occurs at high SZA and high SLA. As can be seen in Fig. 10, ozone values near the morning terminator are probably too low compared to the middle longitude values. These retrieval errors are partly caused by the effects of spherical geometry that are not properly represented in the TOMRAD radiative transfer calculations.

356 The view of the EPIC instrument from sunrise to sunset at fixed UTC is not the diurnal variation
357 that an instrument on the ground would see from sunrise to sunset. For the ground-based Pandora
358 instrument, the observed changes throughout the day from sunrise to sunset are at varying UTC every
359 80 seconds. Compared to the ground-based viewpoint, EPIC obtains data for a fixed geographic location
360 every 68 minutes UTC in NH daytime summer and every 110 minutes in NH daytime winter.

361 **5.1 Southern Hemisphere SH Late Spring 23 November 2015** :

362 To illustrate the SH synoptic change in ozone, Figs. 10 and 11 show the diurnal (longitudinal)
363 variation of ozone centered on the South American continent on 23 November 2015 at 16:20 UTC. The
364 local time varies from early morning (06:20, -150° longitude) to late-afternoon (16:20, 0° longitude). At
365 high southern latitudes, 60°S and 70°S, the late spring (23 November) residue of 2015 Antarctic ozone
366 hole is clearly visible in the ozone map image (Fig. 10). Figure 11 shows details of the ozone amounts in
367 specified latitude bands (±0.125^O wide) in the Southern Hemisphere sampled every 5° degrees from 0°
368 to 70°S. Solar zenith angles are limited to the range ±70° to avoid high latitudes and longitudes near
369 sunrise or sunset where spherical geometry effects become important. This particular example (Fig. 11)
370 is from one image centered over South America (Fig. 10). For 23 November there are 15 more
371 overlapping images covering the entire 360° of longitude that could be combined to produce a complete
372 composite global map of ozone at 15 different UTCs. In the NH summer there would be 22 images per
373 day. A composite ozone map of this kind would no longer be synoptic, since overlapping data are
374 averaged, but would now be similar to the joined data strips from OMI or OMPS.

375 Figure 11 contains the data points from a 0.25^O x 0.25^O average within each 5° latitude band L
376 shown as light grey dots. The dark lines are a Lowess(0.05) fit (locally weighted least squares fit to 5 % of
377 the data, (Cleveland, 1981)), which corresponds to approximately a 30 minute time average (7.5^O
378 Longitude). The largest apparent scatter from the Lowess fit occurs at L = 0.125^{O}S, which amounts to a
379 longitudinal standard deviation from the mean of ±4 DU or ±1.5 %.The equatorial bands (0°S to 20°S)
380 shows considerable longitudinal change (10–20 % from L = 0–40°S rising to 75 % at L = 70°S,
381 approximately as TCO = 16.063 + 0.56L + 0.02L^2). Most of the observed changes are dynamically driven,
382 since the photochemistry involved in the stratosphere (20 - 25 km altitude) is too slow to produce such
383 large changes with changing SZA. Southward of 45°S, the effects of the remaining ozone hole depletion
384 (dark blue in Fig. 10), which is still present in November, appear at -50° longitude as indicated in Fig. 11.

385 **5.2 Northern Hemisphere NH Summer Solstice 21 June 2016:**

386 An example is provided for the ozone retrievals obtained on 21 June 2016 at 18:41 UTC that is
387 approximately centered over North America (Fig. 12). Since this is Northern Hemisphere summer
388 solstice, corresponding to the sun being nearly overhead at 23°N, the latitude range available for
389 retrieving ozone extends over the North Pole. Figure 13 contains ozone retrievals in 0.25^O wide latitude
390 bands similar to Fig. 11. Unlike the SH 23 November 2015 example, there is only moderate longitudinal
391 (diurnal) variability in ozone amount for latitudes between 0° and 15°N. However, there is a clear wave
392 structure in the 20°N to 25°N bands with a periodicity of approximately 35° longitude (2.3 hours) and
393 again in the 40°N to 60°N bands that are not obvious in the global map (Fig. 12).

394   The dynamical effects on ozone in the NH mid-latitudes are quite different than their
395   counterparts in the SH, where the NH mid-latitude behavior (30°N–35°N) is clearly separated from
396   equatorial and high latitude bands with an increase in ozone amount from about 280 DU to about 350
397   DU, which is larger than a similar increase in the SH. There is an ozone periodicity of approximately 38°
398   longitude (2.5 hours) at 30°N–35°N midday and a longer longitudinal period 73° (4.9 hours) in the
399   morning. At higher latitudes, 35°N–55°N, the variability is more pronounced with an approximate
400   period of 55° (3.6 hours). In the bands from 55°N–70°N the variability is reduced and the ozone amount
401   falls from mid-latitude values of about 350 DU to below 300 DU. The wave structure varies throughout
402   the year in both hemispheres.

403   **5.3 Northern and Southern Hemisphere 17 April 2016 18:35 UTC**

404   Figure 5-5 shows the ozone retrieval for the sunlit globe on 17 April 2016 at 18:36 UTC about 1
405   month from the March equinox including large plumes of elevated ozone amounts (450 DU) extending
406   from high latitudes into mid-latitudes where the usual ozone amount is about 350 DU. For the SH (Fig. 5-
407   5), polar ozone variability (280-320 DU) is relatively small compared to November 23 (Fig. 10). There is
408   wave structure (Fig. 15) between 30°S and 40°S with a periodicity of about 4 hours (60° longitude) (see
409   also Schoeberl and Kreuger, 1983). The dip in O$_3$ amount at 77°W to 67°W and 10°S to 25°S
410   corresponds to the Andes Mountains in Peru, Bolivia, and Chile. While the SZA range is limited to ±70°,
411   the SLA reaches more than 80° at low latitudes for longitudes between 40°S and 20°S introducing
412   spherical geometry correction errors that increase towards sunset near 20°W. The errors appear as
413   apparent increases in O$_3$ amount. At higher latitudes, the SLA is in the middle 70°s when the SZA is 70°.
414   The high SLA error is present in both hemispheres for observations near equinox.

415   The NH shows little variability in the equatorial region (0–25°N) with a mean value of about 260
416   DU (Fig. 16). The SLA error is present for latitudes between 0 and 15°N and 0 and 15°S that appears as
417   an elevated ozone amount at longitudes east of 50°W. Mid-latitudes (30°N to 40°N) show a wave
418   structure that is approximately 37° apart (2.5 hours) at 35°N. A similar structure occurs in the SH with a
419   period of about 4.5 hours. There is an ozone maximum (red area in Fig. 14 about 450 DU) near 140°W
420   extending from 60°N to 35°N, very high ozone amounts in the Arctic region, and a high ozone patch
421   over the central US (35°N to 45°N and 104°W) peaking at 420 DU (40°N and 104°W), which probably
422   corresponds to a region of high atmospheric pressure.

423   **6.0 Estimating Erythemal Irradiance at the Earth's Surface**

424   The unique observing geometry of DSCOVR/EPIC permit the use of synoptic ozone and cloud
425   reflectivity data to be used to compute the diurnal variation of UV irradiance from sunrise to sunset for
426   any point on the illuminated earth observed by EPIC. Previous calculations from satellite data used
427   cloud cover and ozone from 13:30 and assumed it applied to local noon. The assumption is usually
428   adequate for slowly varying ozone, but not for estimating the effects of more rapidly varying cloud
429   cover. The following paragraphs discuss the calculation of erythemal irradiance, a spectrally weighted
430   mixture of UV wavelengths used as a measure of skin reddening and potential sunburn from exposure to
431   sunlight.

432   Erythemal irradiance E_0(SZA θ, C_T) at the earth sea level (watts/m^2) is defined in terms of a
433   wavelength dependent weighted integral over a specified weighting function A(λ) times the incident
434   solar irradiance I(λ,θ,Ω,C_T) (Watts/m^2) (Eq. 11) at the Earth's sea level. The erythemal weighting function
435   Log_{10}(A_{ERY}(λ)) is given by the standard Erythemal fitting function shown in Eq. 12 (McKinley and Diffey,
436   1987). Tables of radiative transfer solutions for D_E = 1 AU are generated for a range of sza (0 < θ < 90°),
437   for ozone amounts 100 < Ω < 600 DU, and terrain heights 0 < Z < 5 km using the TUV DISORT radiative
438   transfer model as described in Herman (2010) for erythemal and other action spectra (e.g., plant
439   growth, vitamin D production, cataracts, etc.).

$$E_0(\theta,\Omega,C_T) = \int_{250}^{400} I(\lambda,\theta,\Omega,C_T)A(\lambda)d\lambda \qquad (11)$$

250 < λ < 298 nm	Log_{10}(A_{ERY}) = 0 (12)
298 < λ < 328 nm	Log_{10}(A_{ERY}) = 0.094 (298 - λ)
328 < λ < 400 nm	Log_{10}(A_{ERY}) = 0.015 (139 - λ)

440   Equation 11 can be accurately approximated by the power law form (Eq. 13), where U(θ) and R(θ)
441   are fitting coefficients to the radiative transfer solutions in the form of rational fractions. Rational
442   fractions were chosen because they tend to behave better at the ends of the fitting range than
443   comparable fitting accuracy polynomials.

$E_0(\theta,\Omega,C_T)$ = U(θ) (Ω/200)$^{-R(\theta)}C_T$ (13)

U(θ) or R(θ) = (a+cθ^2+ex^4)/(1+bθ^2+dθ^4+fθ^6)   r^2 > 0.9999   (14)

C_T = (1-LER)/(1-R_G) where R_G is the reflectivity of the surface   (15)

E(θ,Ω,Z) = E_0(θ,Ω) H(θ,Ω,z)   (16)

H(θ,Ω,Z) = 1+(0.04652 Z_{km} +0.00496) (-0.07033 (Ω/200) + 1.12303)G(θ)   (17)

G(θ) = g+hθ+iθ^2+jθ^3+kθ^4 (18)

  The coefficients a, b, c, d, e, f, g, h, j, and k are in Tables A-1 and A-2 in the appendix

444   The E_0 solutions to the radiative transfer calculations can be accurately reproduced by a relatively
445   simple functional form (Eqs. 13 to 15) with the coefficients given in Table A-1. These are the same
446   coefficients given in Herman (2010) along with other biological action spectra weighting functions, H(z,θ)
447   is a function representing the increase in E(θ,Ω,Z) with altitude per km, and C_T is the cloud transmission
448   function (Eq. 15) estimated from the retrieved LER derived by assuming that the cloud-ground system
449   can be approximated by a two-layer Stokes problem (elevated cloud and surface) with atmospheric
450   effects between the cloud bottom and the surface neglected (Herman et al.,2009). r^2 is a measure of
451   the correlation of the E_0 data points with the fitting function. Eqs. 13 to 18 are for an Earth-Sun distance
452   of 1 AU.

453   For E_0 The fitting residual is less than ± 0.001 W/m^2 compared to the worst case when E_0(50°,

454   200) = 0.15 W/m^2 (Herman, 2010). When height effects are included $E(\theta,\Omega,Z)$ = $E_0(\theta,\Omega)$ $H(\theta,\Omega,Z)$,

455   where $H(\theta,\Omega,Z)$ is a fitting polynomial (Eq. 17) to the downward irradiance at 0, 1, 2, 3, 4, and 5 km

456   based on results from the radiative transfer calculation. The increase of erythemal irradiance with

457   altitude has an SZA dependence given by $G(\theta)$, which increases with θ until θ is approximately 60°, and

458   then $G(\theta)$ decreases.

459   The height dependence of $E(\theta,\Omega,Z)$ is similar to that derived by Chubarova et al. (2016) for low

460   aerosol amounts. When absorbing aerosols have a significant optical depth, Chubarova et al. (2016)

461   derived a multiplicative correction term to $E(\theta,\Omega,Z)$ for a wide variety of conditions.

462

463   When Eq. 13 is applied to the ozone and LER data described in previous sections, the global

464   erythemal irradiance at the ground can be obtained after correction for the Earth-Sun distance D_E in a

465   manner similar to Eq. 1, where D_E in AU can be approximated by (Eq. 19),

466

$$D_E = 1 - 0.01672 \cos(360 \, (day\_of\_year - 4)/365.25) \qquad\qquad (19)$$

467

468   An example of $E(\theta,\Omega,Z)$ is shown in Fig. 17 for 17 April 17 2016 at 18:35 UTC. Local noon is near

469   the center of the image with sunrise to the left (west) and sunset to the right (east). For this date, the

470   sun is overhead just north of the equator producing very high values of Erythemal irradiance $E(\theta,\Omega,Z)$

471   corresponding to a UV index, UVI, of 13 at sea level in the Pacific Ocean (UVI = 40 $E(\theta,\Omega,Z)$). The UVI

472   scale was designed for sea level mid latitudes ranging from 0 to 10 to provide public health warnings

473   (e.g. for UVI = 8). Somewhat higher values are seen in the Sierra Nevada Mountains in Mexico near

474   20°N. This particular day is relatively cloud free over most of South America except for clouds over

475   southern Brazil extending into Paraguay and other small patches of clouds. For the erythemal irradiance,

476   the presence of clouds reduces the amount of UV reaching the ground (blue color with a UV index of

477   less than 4).

478

479   The increase with altitude is much more pronounced during the summer months over the Andes

480   Mountains reaching above 4 km (over 13,000 feet). Figures 18 and 19 show the large increases with

481   altitude over the Andes Mountains for 23 November 2015, with the sun nearly overhead at 20°S

482   latitude. Here the UV index ranges from 16 to 18, which agrees with previous ground-based

483   measurements in this region (Cede et al., 2002). Any significant unprotected exposure to these levels of

484   UV would lead to severe sunburn and eye damage. On a completely clear day the UV index would be

485   even higher than 18. Figure 19 is a longitudinal slice through the UV data in Fig. 18 at 20°S. The figure

486   shows the longitudinal variation $E(\theta,\Omega,Z)$ as a function of local time, the effect of light clouds on the

487   eastern side of the Andes Mountains, and the sharp reduction at 50°W.

488

489   Figure 20 shows the erythemal irradiance computed for 21 June 2016 centered over the US and

490   Central America. The sun is overhead at 23.3^{O}N latitude. In the clear regions not covered with light

491   clouds, the UV index reaches about 12 extending from an area in the Pacific Ocean at 15°N up into the

492   US mid-west, Rocky Mountains, Utah and New Mexico. The eastern US has a lower UV index of about 8.

493 The extended scale of this map (UVI = 0 to 20) is too coarse to see the variation with latitude on the east
494 coast.

495

496   Similarly, Fig. 21 shows high values of Erythemal irradiance in the Himalayan Mountains on June
497 21, 2016 with peak UV index of about 15 even in the presence of partial cloud cover that reflects a
498 portion of the incident solar flux back to space. The effect of cloud cover can be seen in Fig. 22, which is
499 a longitudinal slice through the irradiance values associated with the latitude at 32^ON. In the absence of
500 clouds, the peak value of the UV index would be close to 20. Even with cloud cover, the UV index
501 reached 15, which is twice the value of a typical cloudless summer case in the US at comparable
502 latitude.

503   **7.0 Summary**

504   The DSCOVR/EPIC 10-filter Spectroradiometer (317.5 to 780 nm) makes measurements of the
505 the rotating sunlit face of the earth from the Lagrange-1 point located 1.5×10^6 km from the earth with a
506 maximum resolution of 10 x 10 km^2 for 443 nm at the sub-satellite point. The other 9 channels have 18 x
507 18 km^2 resolution. The key difference between EPIC and LEO satellites is EPIC's ability to measure the
508 whole sunlit earth (sunrise to sunset) at the same UTC (synoptic measurements) every 68 or 110
509 minutes depending on the season at the Wallops Island, Virginia data receiving station. EPIC ozone
510 retrievals have been compared successfully to both ground-based Pandora spectrometer instruments
511 and to the MERRA-2 satellite data assimilation model for the same UTC observed by EPIC.   EPIC's
512 synoptic measurements insure that the ozone amounts, cloud reflectivity, and aerosol amounts that are
513 used to estimate UV irradiance are the proper values for each time of the day. EPIC has been making
514 measurements since June 15, 2015 with no evidence of significant degradation relative to LEO satellites
515 observing the same scene at the same angles. EPIC has obtained ozone and reflectivity data multiple
516 times per 24 hours for over two years that can be used to more accurately estimate the health effects
517 from continuous or periodic exposure during any day to UV radiation reaching the ground including the
518 effects of cloud cover and altitude.

519

520

521

522

523

524

525

526

527 **Appendix**

528 Figure A1 illustrates the orbit of the DSCOVR spacecraft following the earth in its orbit about the
529 sun.

530

Table A-1 Coefficients R(θ) and scaling coefficient U(θ) for $0 < \theta < 80^O$
and $100 < \Omega < 600$ DU for $E(\Omega,\theta) = U(\theta) (\Omega/200)^{-R(\theta)}$ ($1.0E10 = 1.0 \times 10^{10}$)

$U(\theta)$ or $R(\theta) = (a+c\theta^2+e\theta^4)/(1+b\theta^2+d\theta^4+f\theta^6)$ $r^2 > 0.9999$

Action Spectra	$U(\theta)$ (watts/m^2)	$R(\theta)$
CIE Erythemal U_{ERY} & R_{ERY}	a= 0.4703918683355716 b= 0.0001485533527344676 c= -0.0001188976502179551 d= 1.915618238117361E-08 e= 7.693069873238405E-09 f= 1.633190561844982E-12	a= 1.203020609002682 b= -0.0001035585455444773 c= -0.00013250509260352 d= 4.953161533805639E-09 e= 1.897253186594168E-09 f= 0.0

Table A-2 Solar Zenith angle function G(θ) used in Eq. 18

$G(\theta)$ = $g+h\theta+i\theta^2+j\theta^3+k\theta^4$

g= 0.9996074048174048   j= 1.412462444962443E-06
h= 0.0001453776871276851   k= -2.037907925407924E-08
i= 2.806514180264192E-05

531

532

533

534

535

536

537

538

539

540

References

Bodrogi, Peter and Tran Quoc Khanh, Illumination, Color and Imaging: Evaluation and Optimization of Visual Displays, Wiley-VCH Verlag GmbH & Co. KGaA. 2012.

Brion, J., Chakir, A., Daumont, D., Malicet, J., and Parisse, C.: High-resolution laboratory absorption cross section of O3. Temperature effect, Chem. Phys. Lett., 213, 610–612, 1993.

Brion, J., Chakir, A., Charbonnier, J., Daumont, D., Parisse, C., and Malicet, J.: Absorption spectra measurements for the ozone molecule in the 350–830 nm region, J. Atmos. Chem., 30, 291–299, 1998.

Broadbent, Arthur D. A critical review of the development of the CIE1931 RGB color-matching functions, Color Research & Applications. 29 (4): 267–272. doi:10.1002/col.20020, 2004

Cariolle, D., and M. Déqué (1986), Southern hemisphere medium-scale waves and total ozone disturbances in a spectral general circulation model, J. Geophys. Res., 91(D10), 10825–10846, doi:10.1029/JD091iD10p10825 1986.

Caudill, T.R., D.E. Flittner, B.M. Herman, O. Torres, and R.D. McPeters, Evaluation of the pseudo-spherical approximation for backscattered ultraviolet radiances and ozone retrieval, J. Geophys. Res., 102, 3881-3890, 1997.

Cede, A., E. Luccini, R.D. Piacentini, L. Nuñez, and M. Blumthaler, Monitoring of Erythemal Irradiance in the Argentine Ultraviolet Network, J. Geophys. Res., 107 (D13), 10.1029/2001JD001206, 2002.

Cleveland, William S., LOWESS: A program for smoothing scatterplots by robust locally weighted regression. The American Statistician. *35 (1): 54.* JSTOR 2683591. doi:10.2307/2683591, 1981.

Daumont, D., Brion, J., Charbonnier, J., and Malicet, J.: Ozone UV spectroscopy I: Absorption cross-sections at room temperature,J. Atmos. Chem., 15,145–155, 1992.

Dobber, M., Voors, R., Dirksen, R., Kleipool, Q., and Levelt, P., 2008, The high resolution solar reference spectrum between 250 and 550 nm and its application to measurements with the Ozone Monitoring Instrument. Solar Phys., 249, 281–291, 2008.

573

574 Gardner, James L., Comparison of Calibration Methods for Tristimulus Colorimeters, Journal of Research

575 of the National Institutes of Standards and Technology. **112** (3): 129–138. doi:10.6028/jres.112.010,

576 2007.

577

578 Herman, J.R., G. Labow, N.C. Hsu, D. Larko (2009), Changes in Cloud Cover (1998-2006) Derived From

579 Reflectivity Time Series Using SeaWiFS, N7-TOMS, EP-TOMS, SBUV-2, and OMI Radiance Data, J.

580 Geophys. Res., 114, D01201, doi:10.1029/2007JD0008, 2009.

581

582 Jaross, G., P. K. Bhartia, G. Chen, M. Kowitt, M. Haken, Z. Chen, P. Xu, J. Warner, and T.

583 Kelly (2014), OMPS Limb Profiler instrument performance assessment, J. Geophys. Res.

584 Atmos., 119, 4399–4412, doi:10.1002/2013JD020482, 2014.

585

586 Madronich, S., McKenzie, R.L., Björn, L.O. and Caldwell, M.M. (1998), "Changes in biologically active

587 ultraviolet radiation reaching the Earth's surface," *Photochem. Photobiol.* **46**, 5-19, 1998.

588

589 Malicet, J., Daumont, D., Charbonnier, J., Chakir, C., Parisse, A.,and Brion, J.: Ozone UV Spectroscopy.II:

590 Absorption cross sectionsand temperature dependence, J. Atmos. Chem., 21, 263–273, 1995.

591

592 Marshak, A., T., Várnai, and A., Kostinski (2017), Terrestrial glint seen from deep space: Oriented ice

593 crystals detected from the Lagrangian point, Geophys. Res. Lett., 44, doi:10.1002/2017GL073248, 2017.

594

595 McKinley, A. F., and B. L. Diffey (1987), A reference action spectrum for ultraviolet induced erythema in

596 human skin, in Human Exposure to Ultraviolet Radiation: Risks and Regulations, edited by W. R.

597 Passchier and B. F. M. Bosnjakovic, pp. 83 – 87, Elsevier, Amsterdam, 1987.

598

599 Molod, A., Takacs, L., Suarez, M., and Bacmeister, J., 2014: Development of the GEOS-5 atmospheric

600 general circulation model: evolution from MERRA to MERRA-2, Geosci. Model Dev. Discuss., 7, 7575-

601 7617, doi:10.5194/gmdd-7-7575-2014.

602

603 Rodriguez, Juan V., ; Colin J. Seftor ; Charles G. Wellemeyer and Kelly Chance (2003), "An overview of the

604 nadir sensor and algorithms for the NPOESS ozone mapping and profiler suite (OMPS)", Proc. SPIE 4891,

605 Optical Remote Sensing of the Atmosphere and Clouds III, 65 (April 9, 2003); doi:10.1117/12.467525;

606 http://dx.doi.org/10.1117/12.467525, 2003.

607

608 Rotman, D.A., J.R. Tannahill, D.E. Kinnison, P.S. Connell, D. Bergmann, D. Proctor, J.M. Rodriguez, S.J.

609 Lin, R.B. Rood, M.J. Prather, P.J. Rasch, D.B. Considine, R. Ramaroson, S.R. Kawa (2001), The Global

610 Modeling Initiative assessment model: Model description, integration and testing of the transport shell,

611 J. Geophys. Res., 106, 1669-1691, 2001.

612

613 Schoeberl, M.A. and A. J. Krueger, Medium Scale Disturbances in Total Ozone During Southern

614 Hemisphere Summer," *Bull. Amer. Met. Soc.,* 1358, 1983.

615

616 Tzortziou, M., **J. R.** Herman, A. Cede, and N. Abuhassan (2012), High precision, absolute total column

617 ozone measurements from the Pandora spectrometer system: Comparisons with data from a Brewer

618 double monochromator and Aura OMI, J. Geophys. Res., 117, D16303, doi:10.1029/2012JD017814,

619 2012.

620

621 Wargan, Krzysztof, Gordon Labow and Stacey Frith, Steven Pawson, Nathaniel Livesey, Gary Partyka,

622 Journal of Climate 30, DOI: http://dx.doi.org/10.1175/JCLI-D-16-0699.1, 2017.

623

624 Wyszecki, Gunther and W. S. Stiles, Color Science: Concepts and Methods, Quantitative Data and

625 Formulae, 2nd Edition, ISBN: 978-0-471-39918-6, John Wiley and Sons, 1982.

626

627 **Tables**

Table 1 Exposure Times for viewing the Earth and Full Moon (Earth side view)

Wavelength	Earth Exposure (ms)	Full Moon Exposure(ms)	Filter Width (nm FWHM)
317.5	654	2500	1
325	442	500	1
340	67	92	2.7
388	87	95	2.6
443	28	100	2.6
551	22	70	3
680	33	105	1.6
688	75	224	0.84
764	101	250	1.0
779.5	49	180	1.8

628

629

630

631

Table 2	πK_M on 1 January 2016		Irradiance at 1 AU
M	λ (nm)	πK_{MO}	$S_M(mW/m^2/nm)$
1	317.478	1.216E-04	819.0
2	325.035	1.111E-04	807.7
3	339.858	1.975E-05	995.8
4	387.923	2.685E-05	1003.

636

637

Table A1   Coefficients $R(\theta)$ and scaling coefficient $U(\theta)$ for $0 < \theta < 80^O$
and $100 < \Omega < 600$ DU   for $E(\Omega,\theta) = U(\theta)\,(\Omega/200)^{-R(\theta)}$ ($1.0E10 = 1.0 \times 10^{10}$)

$$U(\theta) \text{ or } R(\theta) = (a+c\theta^2+e\theta^4)/(1+b\theta^2+d\theta^4+f\theta^6) \quad r^2 > 0.9999$$

Action Spectra $U(\theta)$ (watts/m^2) $R(\theta)$

CIE Erythemal   a= 0.4703918683355716   a= 1.203020609002682
U_{ERY} & R_{ERY} b= 0.0001485533527344676   b= -0.0001035585455444773
                    c= -0.0001188976502179551   c= -0.00013250509260352
                    d= 1.915618238117361E-08   d= 4.953161533805639E-09
                    e= 7.693069873238405E-09   e= 1.897253186594168E-09
                    f= 1.633190561844982E-12   f= 0.0

638

639

Table A2 Solar Zenith angle function G(θ) used in Eq. 18

$$G(\theta) = g+h\theta+i\theta^2+j\theta^3+k\theta^4$$

g= 0.9996074048174048   j= 1.412462444962443E-06
h= 0.0001453776871276851   k= -2.037907925407924E-08
i= 2.806514180264192E-05

640

641

Figure Captions

f01 Filter transmission functions (percent) for the 10 EPIC wavelengths

f02 Normalized calibration functions referenced to its value at 4 Jan 2016 when D_E = 1 au. Average rate of increase is 0.016 per year.

f03 Natural Color EPIC Earth images from June 6 and December 6, 2016 showing the field of view during the respective hemispheric summers. In both of these images, 6-months apart, the EPIC orbit is to the west of the Earth-Sun line causing the west side of the globe (sunrise) to appear brighter than the east side (sunset). Notice the bright specular reflection over Argentina, South America embedded within a cloud feature. This is thought to be from ice crystals in high clouds (Marshak et al., 2017).

f04 EPIC retrieved ozone and LER values for April 17, 2016 at 00:36 UTC. The ozone scale is from 100 to 500 DU, and the LER scale is from 0 to 100 percent.

f05 LER at six sequential UTC 0:36, 2:24, 4:12, 6:00, 7:48, and 9:36 from 17 April 2017 showing clouds in the arctic region as the earth rotates in EPIC's field of view.

f06 Cloud formations from 23 Nov 2015 showing cloud cover in the Southern Hemisphere and near Antarctica at 6 different UTC's, 10:56, 12:44 14:32, and 16:20, 14:32, 18:09, and 19:57.

f07 O_2 A-band View of Antarctica on December 6, 2015 showing clouds over ice. The white bright clouds are at higher altitudes than the dull grey clouds because of a combination of less oxygen absorption and higher optical depth.

f08 Daily O_3 data for EPIC (red) and Pandora (Grey) 2015 - 2016. Left: EPIC ozone data compared to Pandora retrievals at Boulder Colorado. Right: Percent difference between EPIC and Pandora.

f09 Comparison of EPIC total column ozone with the MERRA-2 assimilation model ozone.

f10 Global image of ozone field for Fig. 11 for 23 Nov 2015 at 16:20 UTC

f11 Longitudinal or diurnal variation of ozone for the Southern Hemisphere every 5° degrees from 0° to $70S^O$ for 23 Nov 2015 at 16:20 UTC. The grey points are the individual data points in the band. The solid lines are a Lowess(0.05) fit to the data points representing a solar time average from 0.6 to 0.7 hours depending on latitude. The SZA is limited to $\pm70^O$. Longitude = 0 Corresponds to 16:20 local time and longitude = -150 corresponds to 06:20 local time.

f12 Global image of ozone field for Fig. 13 for 21 June 2016 at 18:41 UTC

f13 Longitudinal or diurnal variation of ozone for the Northern Hemisphere every 5° from 0° to 70° for 21 June 2016 at 18:41 UTC. The grey bands are the individual data points in the band. The solid lines are a Lowess(0.05) fit to the data points representing a solar time average from 0.6 to 0.7 hours depending on latitude. The SZA is limited to $\pm70^O$. Longitude = 0 Corresponds to 18:41 local time and longitude = -180 corresponds to 06:41 local time.

675   f14 Global image of ozone field for Figs. 15 and 16 for 17 April 2016 at 18:36 UTC.

676   f15 Southern Hemisphere: Solid lines are approximately 30 minute averages in solar time at 18:38 UTC
677   on 17 April 2016 for ozone variation between 0° and 55^OS latitude in 0.25^O latitude bands for 17 April
678   2016 at 17:36 UTC.

679   f16 Northern Hemisphere: Solid lines are approximately 30 minute averages in solar time at 18:38 UTC
680   on 17 April 2016 for ozone variation between 0° and 75^ON latitude in 0.25^O latitude bands for 17 April
681   2016 at 17:36 UTC.

682   f17 Erythemal irradiances calculated from Eq. 13 and from the EPIC ozone and LER data obtained on
683   April 17, 2016 at 18:35 UTC. The scale shows both the irradiance values in W/m2 and the UV index
684   ranging from 0 to 20. This scene is centered over the Pacific Ocean and shows a peak UV index of about
685   15. Since this period is close to equinox, the sun is nearly overhead just north of the equator with solar
686   noon at 98.75^OW longitude and overhead near 10^ON.

687   f18 Erythemal irradiances centered over South America on November 23, 2015 at 16:19 UTC showing
688   extremely high values in the Andes Mountains in Peru, Bolivia, and Chile corresponding to a UV index
689   greater than 20. Local solar noon is at 64.75^OW and overhead near 20^OS.

690   f19 Erythemal Irradiances in a longitudinal slice at 20^OS through a peak occurring in the Andes
691   mountains. Local noon is at 64.75^OW.

692   f20 Erythemal irradiances centered over the United States on June 21, 2016 showing high values over
693   the Rocky Mountains and a portions of the Sierra Nevada Mountains. The UV index reaches about 15.
694   Local solar noon is at 99.75^OW and overhead near 23.3^ON.

695   f21 Erythemal UV irradiances centered over the Indian Ocean on June 21, 2016 showing high values over
696   the Himalayan Mountains with the UV index exceeding 14. UV levels are moderated by partial cloud
697   cover reflection of radiation back to space. Solar noon is at 80.25^OE.

698   f22 Erythemal Irradiances in a longitudinal slice at 32^ON through a portion of the Himalayan mountains.
699   Local solar noon is at 80.25^OE.

700   fA1 An illustration of DSCOVR's Lagrange-1 orbit

701

702 **Figures**

703

f01

704
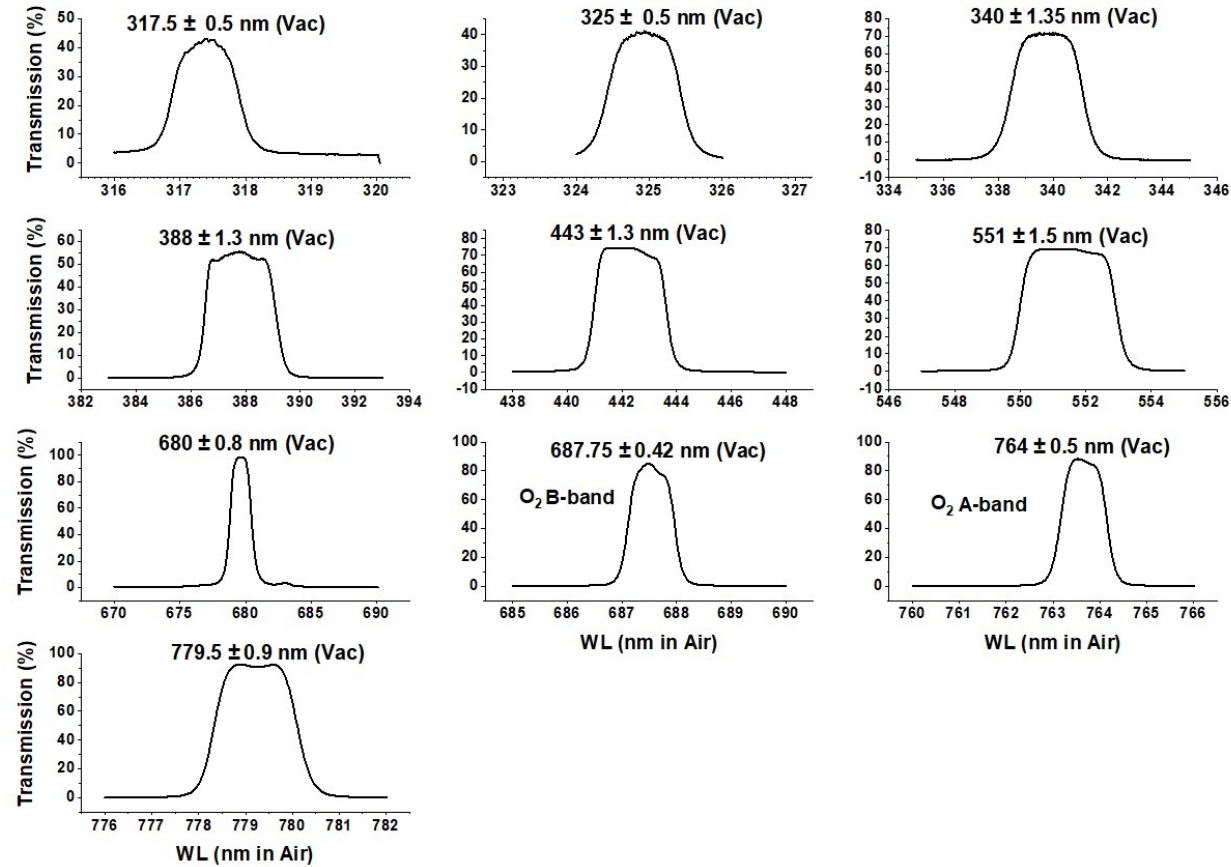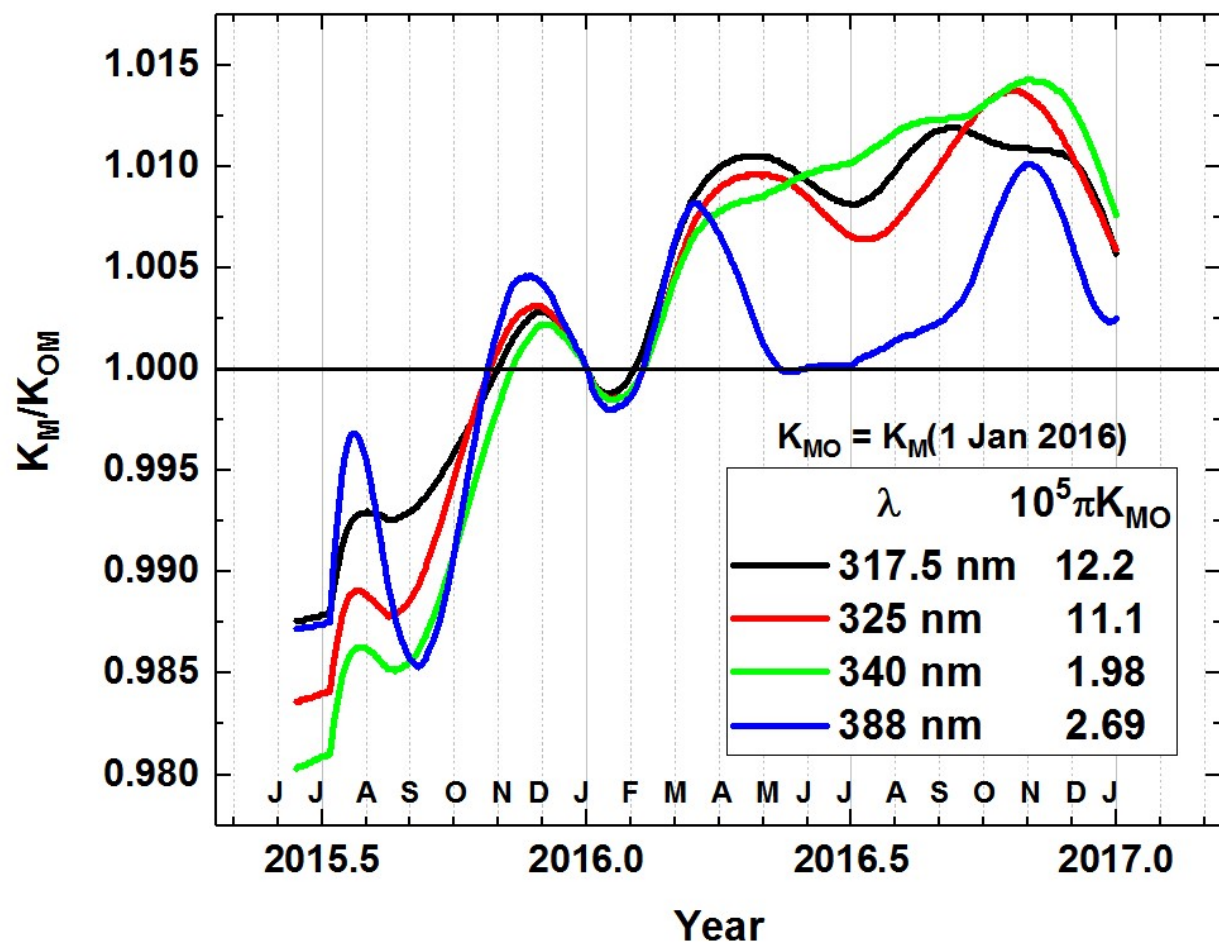
f02

705

706
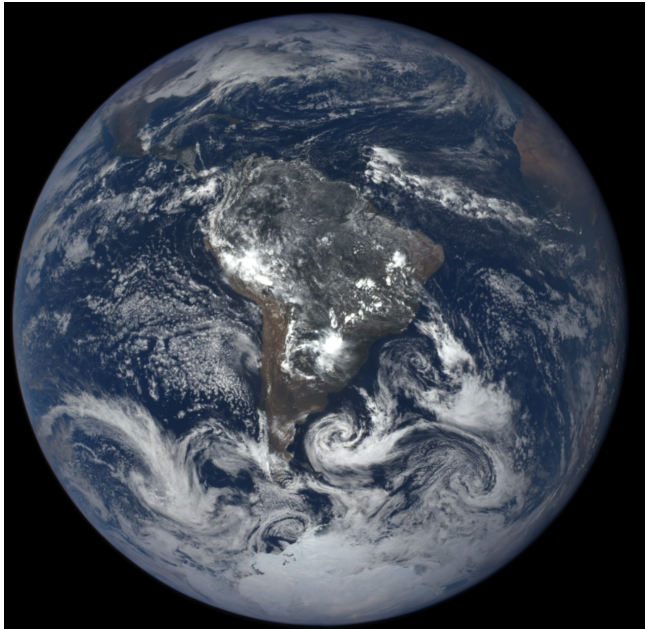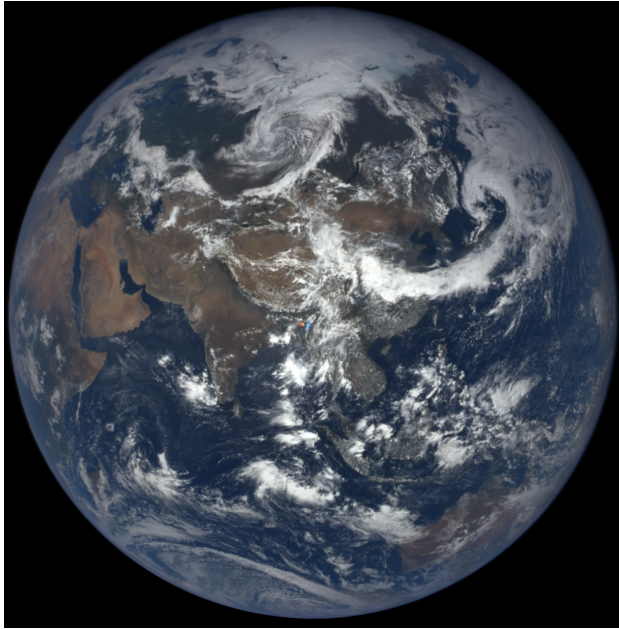
f03

707

708

709

f04

710

711

f05

11/23/15

10:56

12:44

14:32

16:20

18:09

19:57
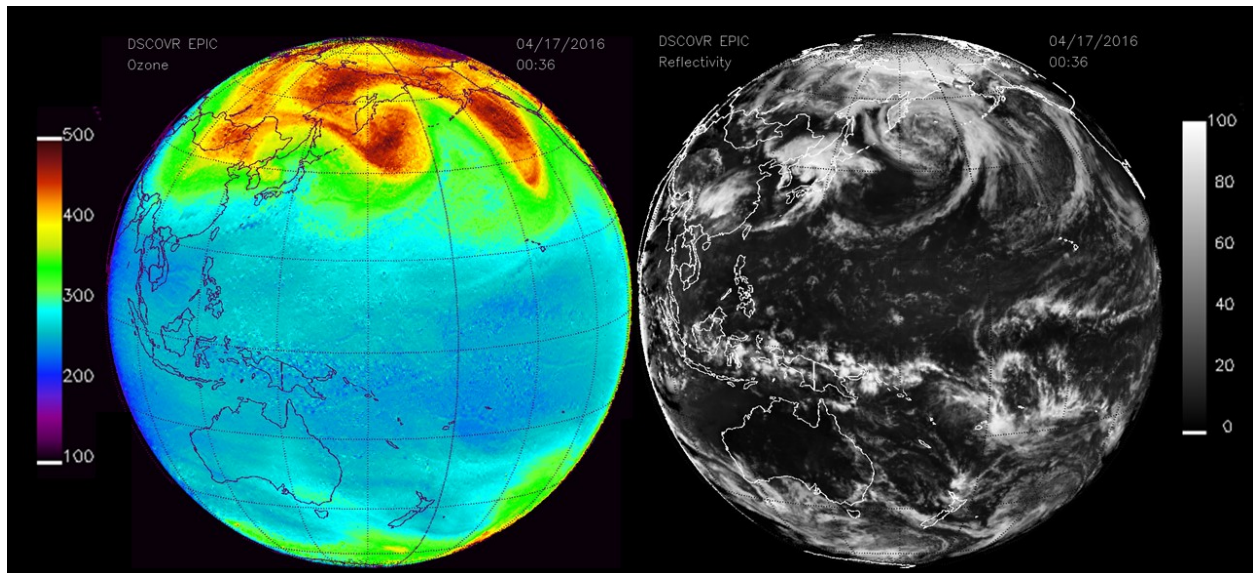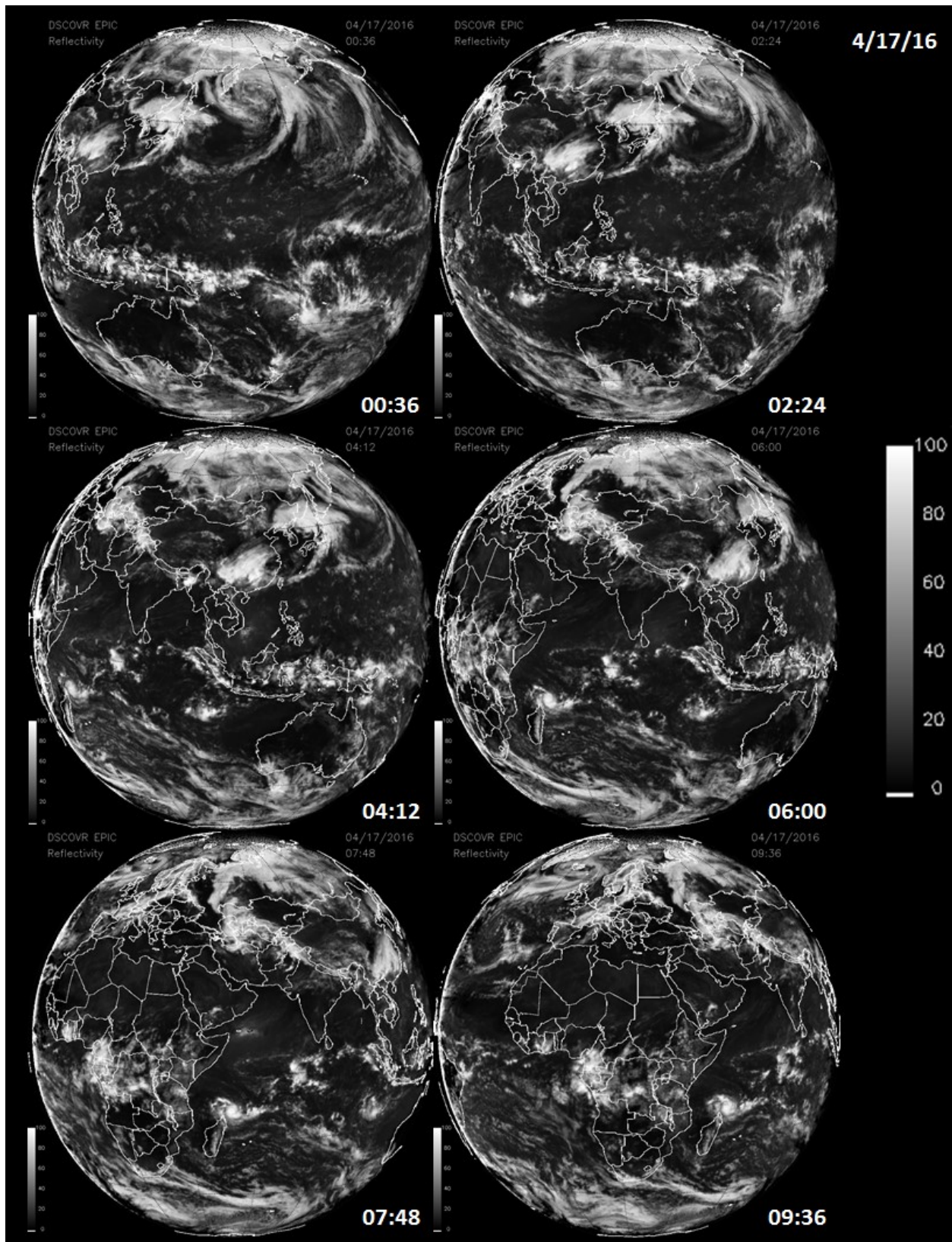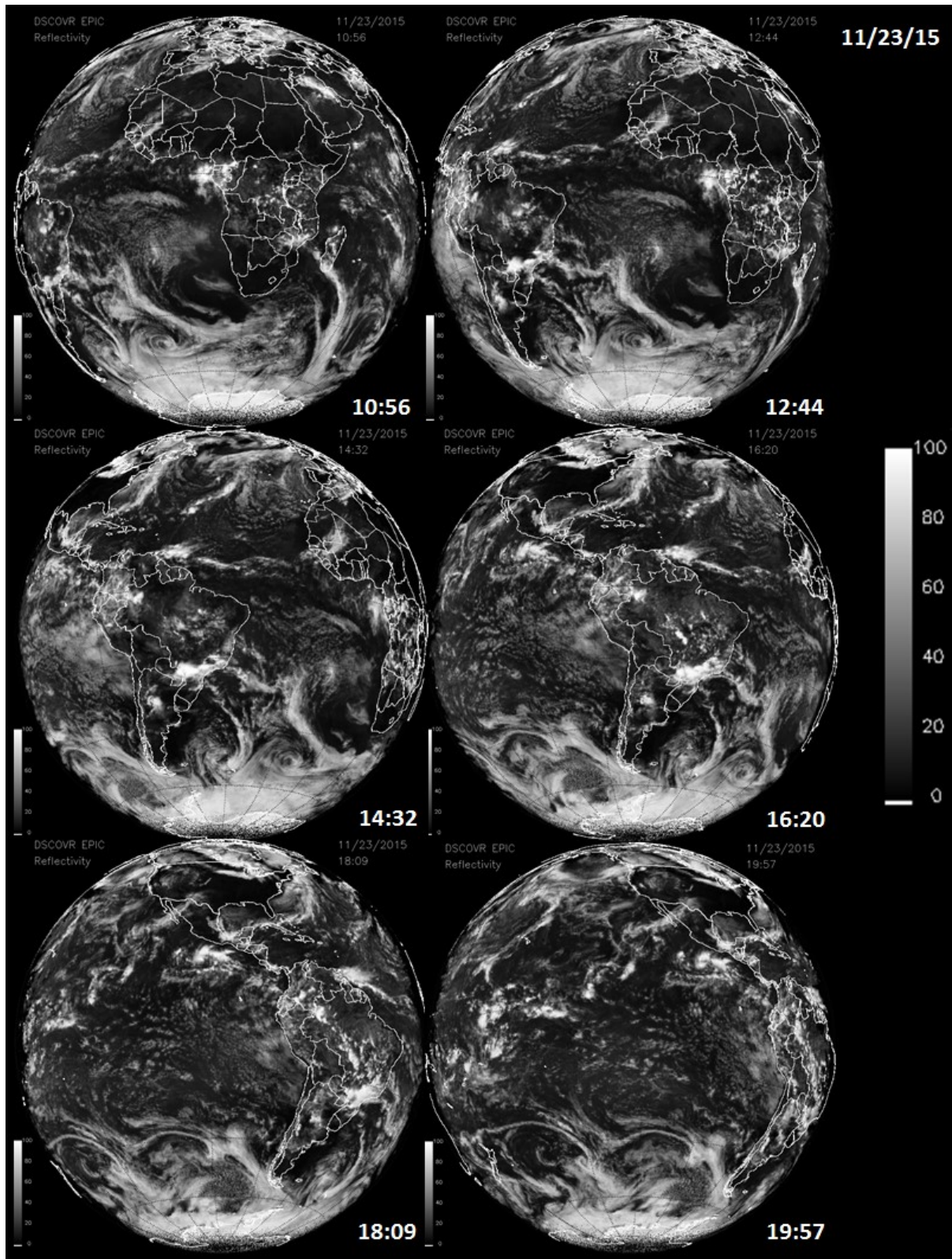
f06

712

713
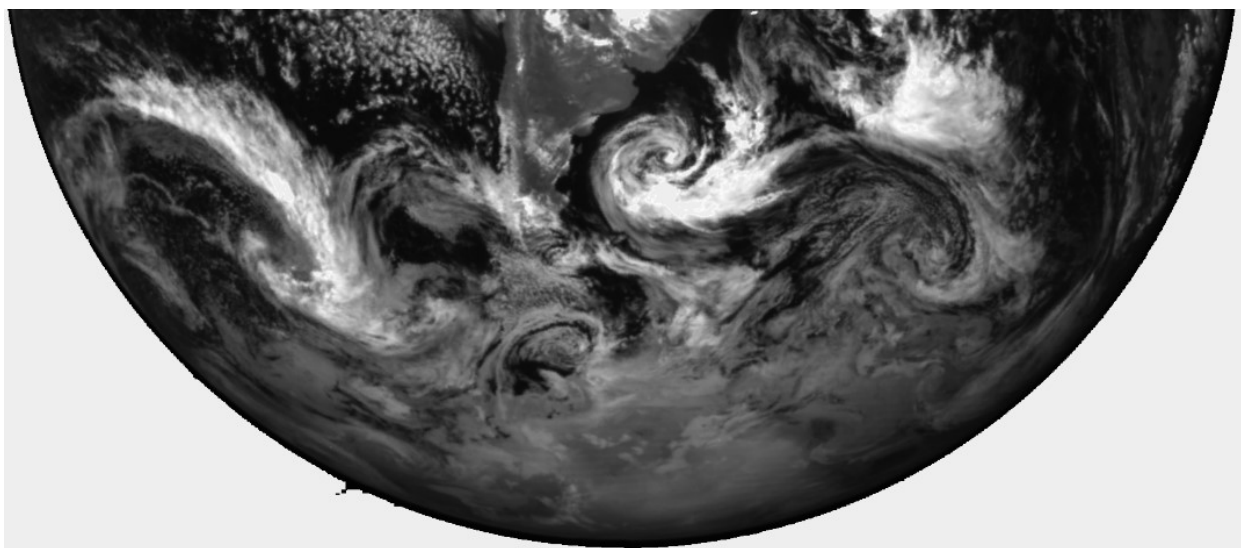
f07

714

715

716

717

718
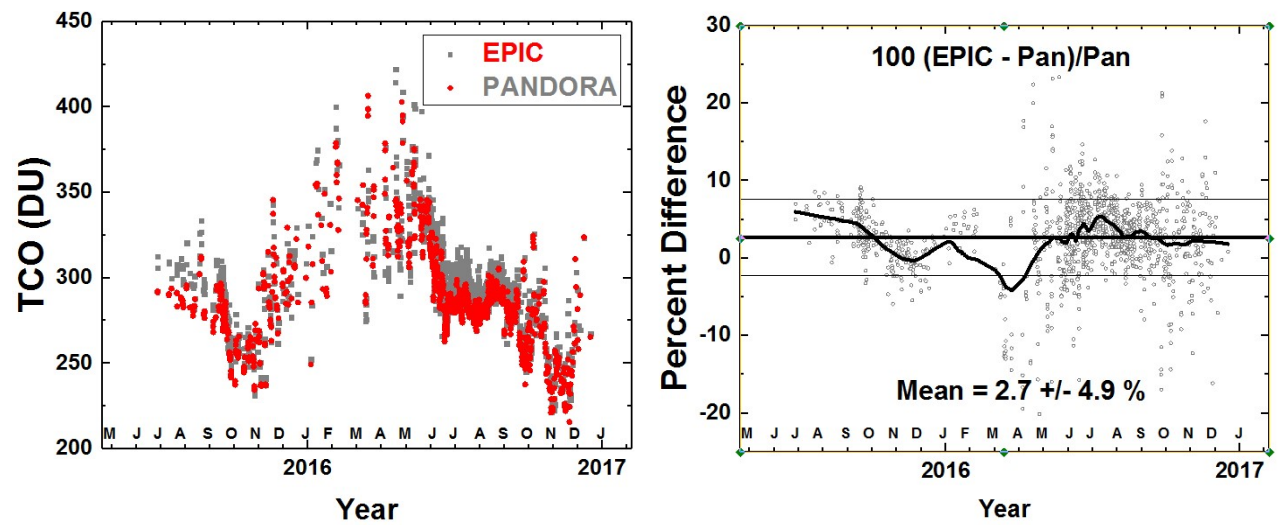
f08

719

f09

f10

722

723

f11

f12

f13

21 June 2016
18:41 GMT
25 x 25 km^2
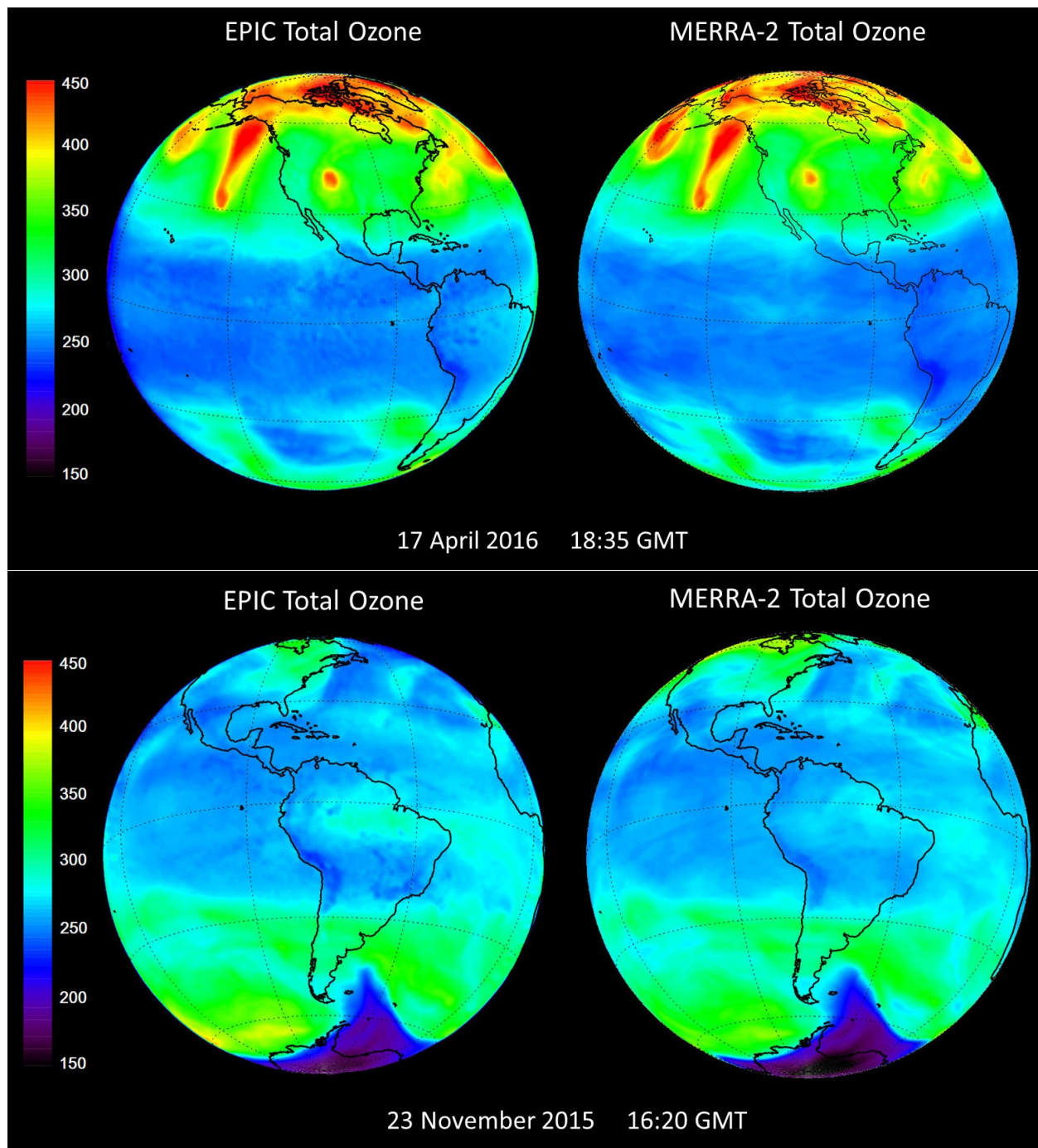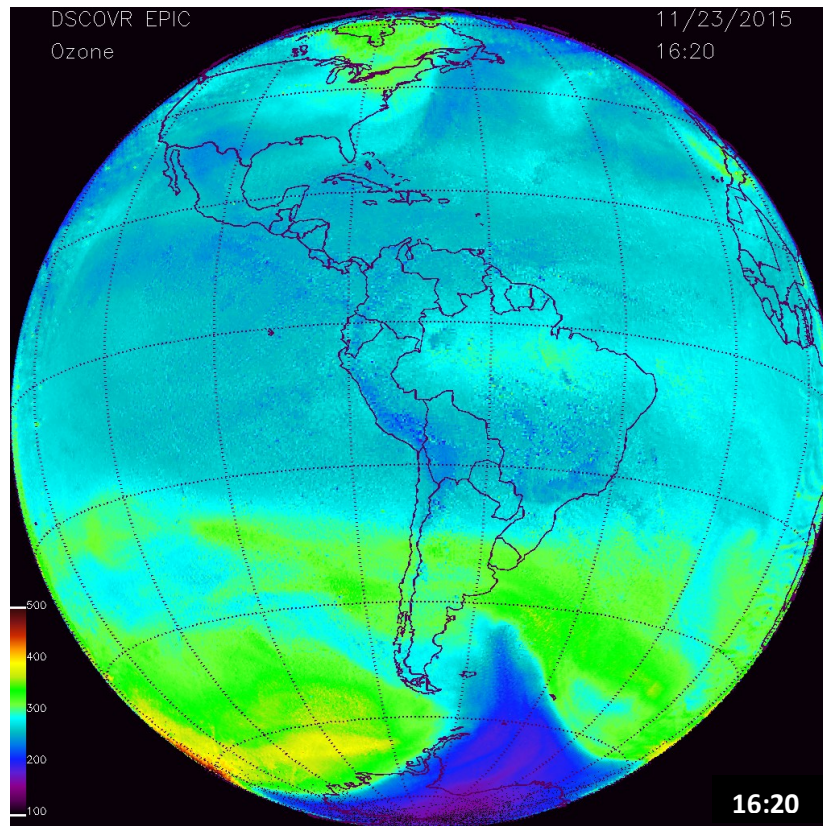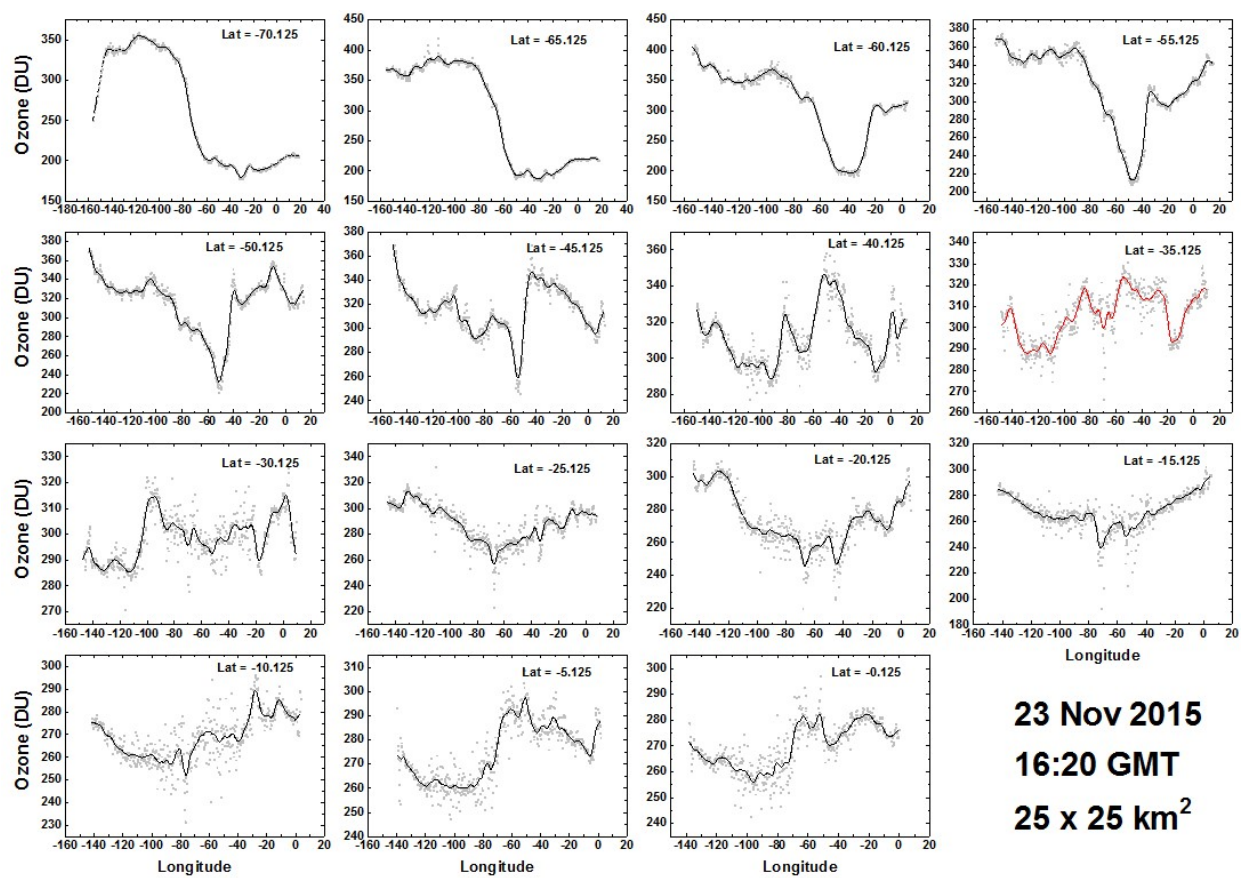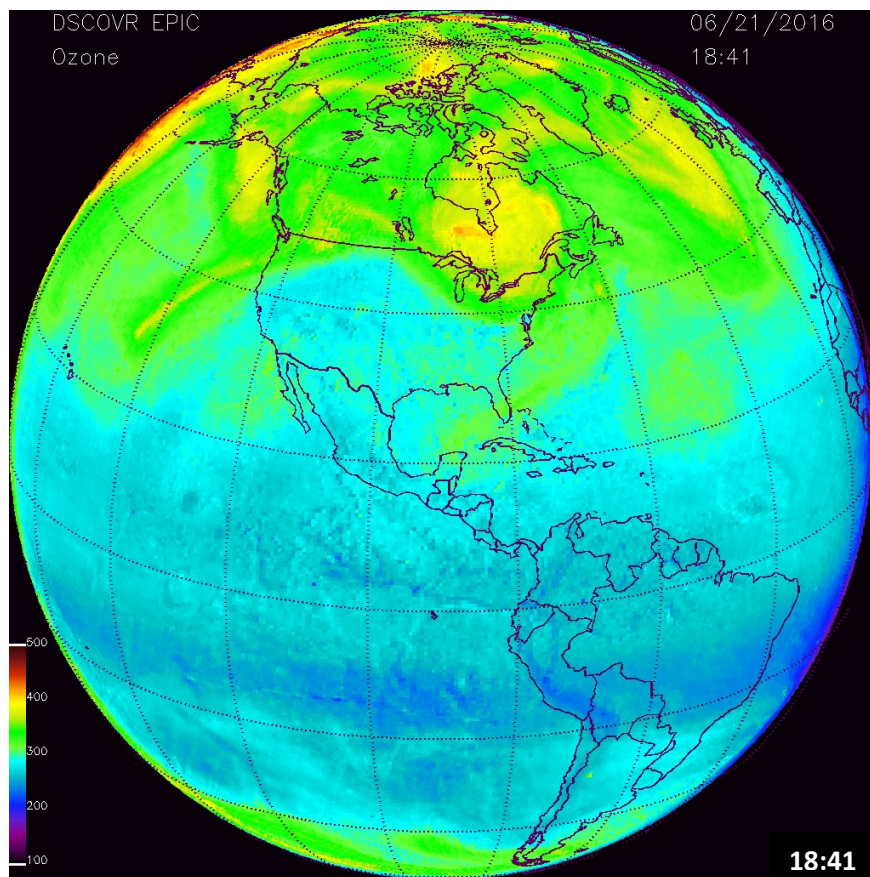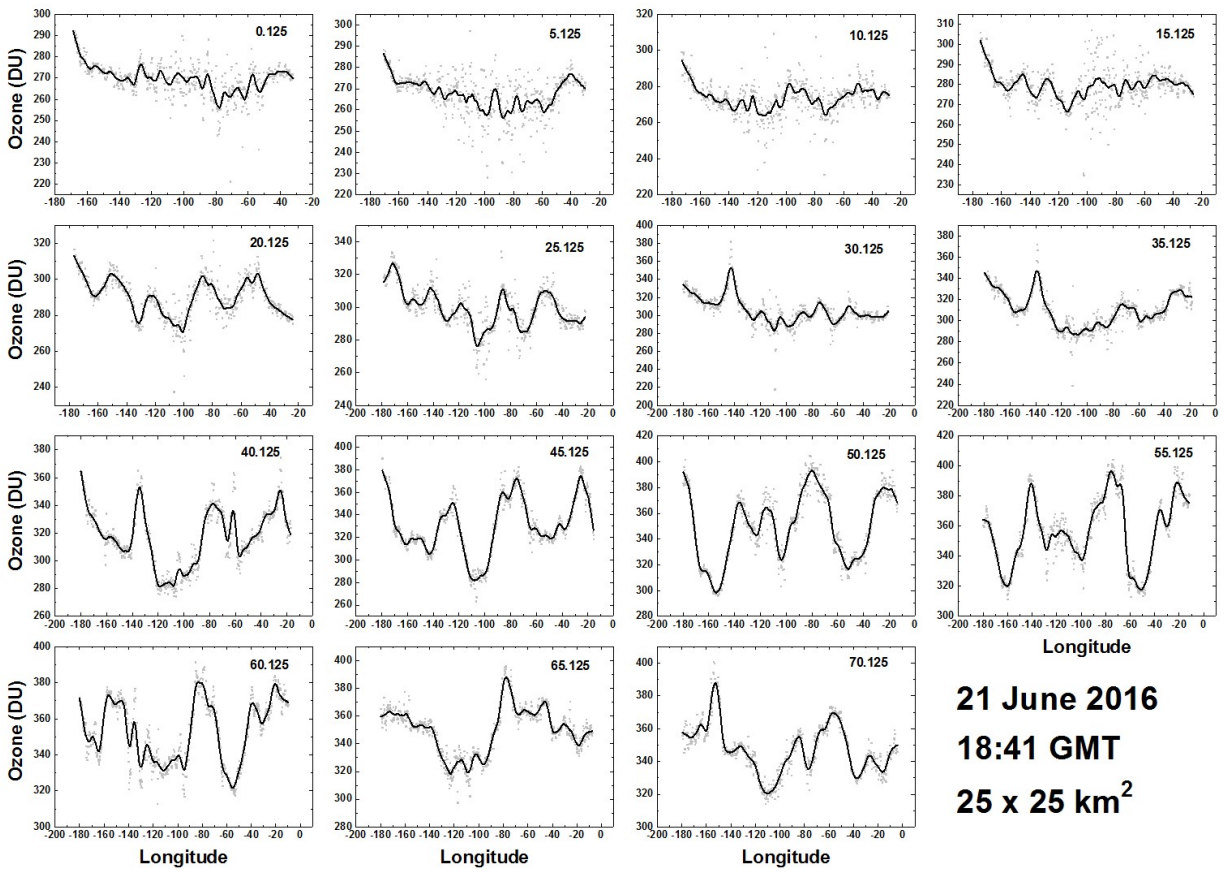
743

744

745

746

747

748

749

750

751

752

f14
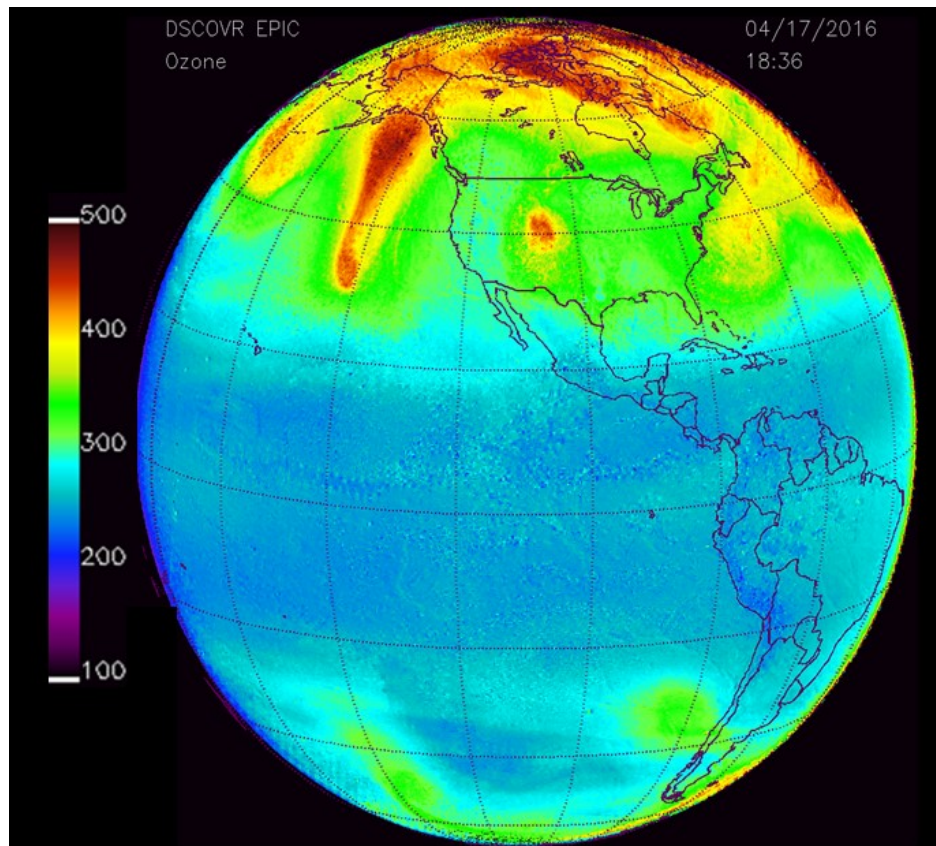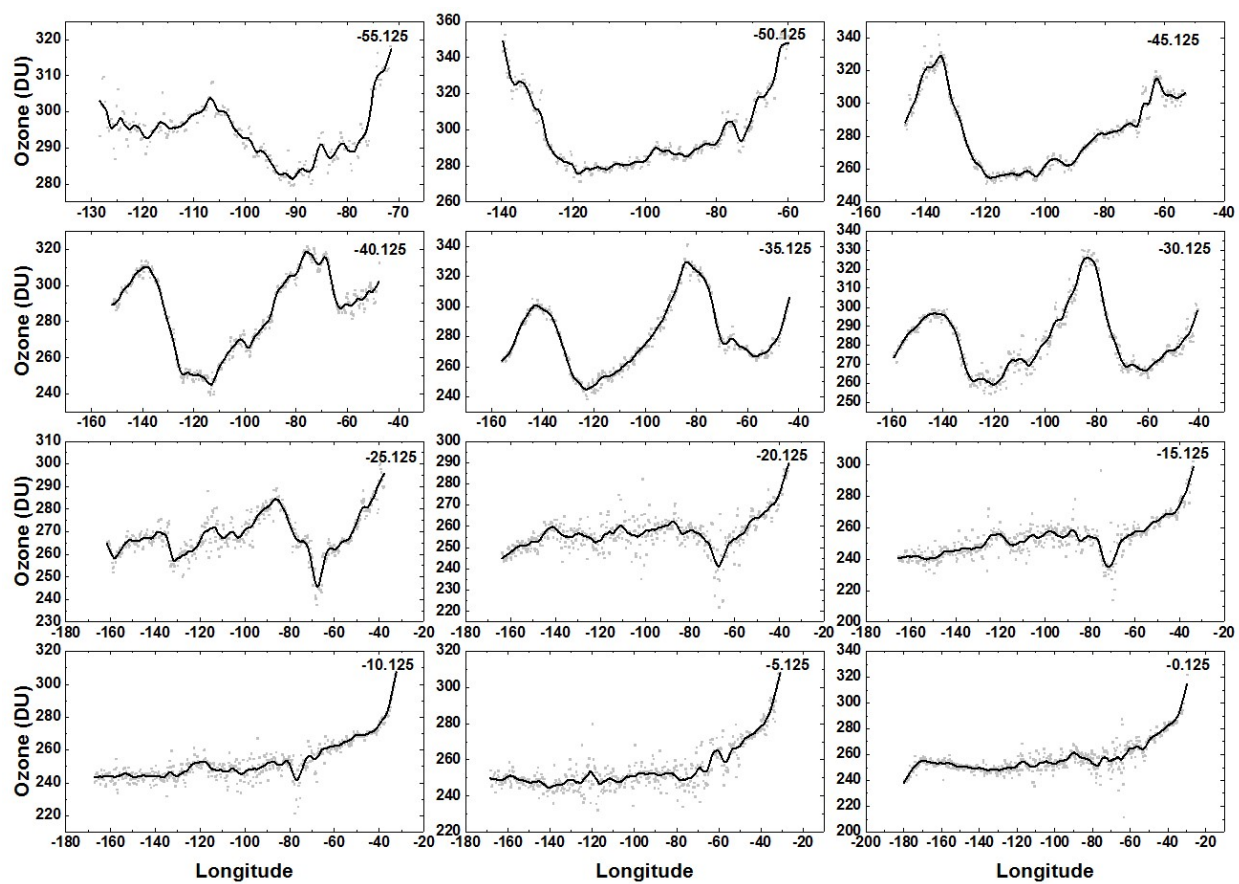
f15
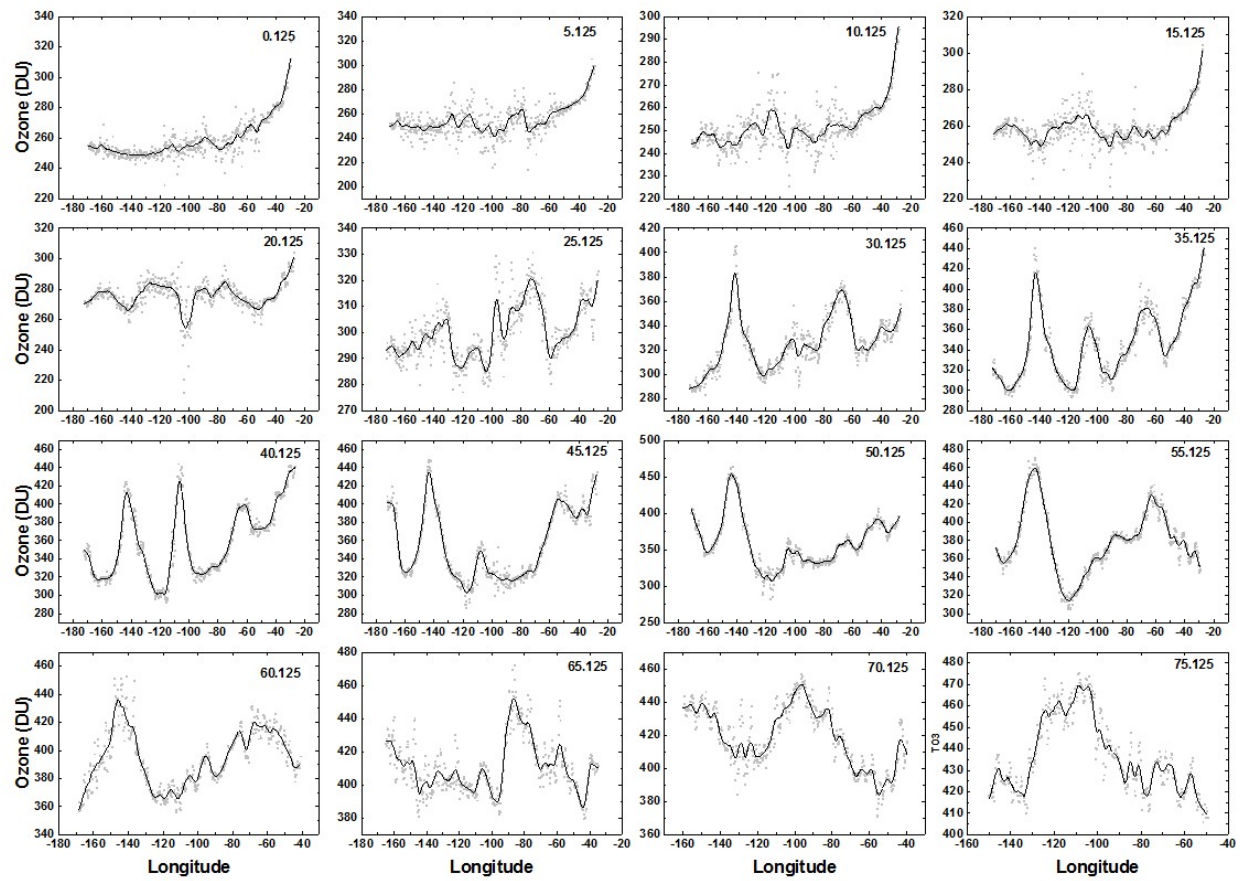
f16

756

757

758
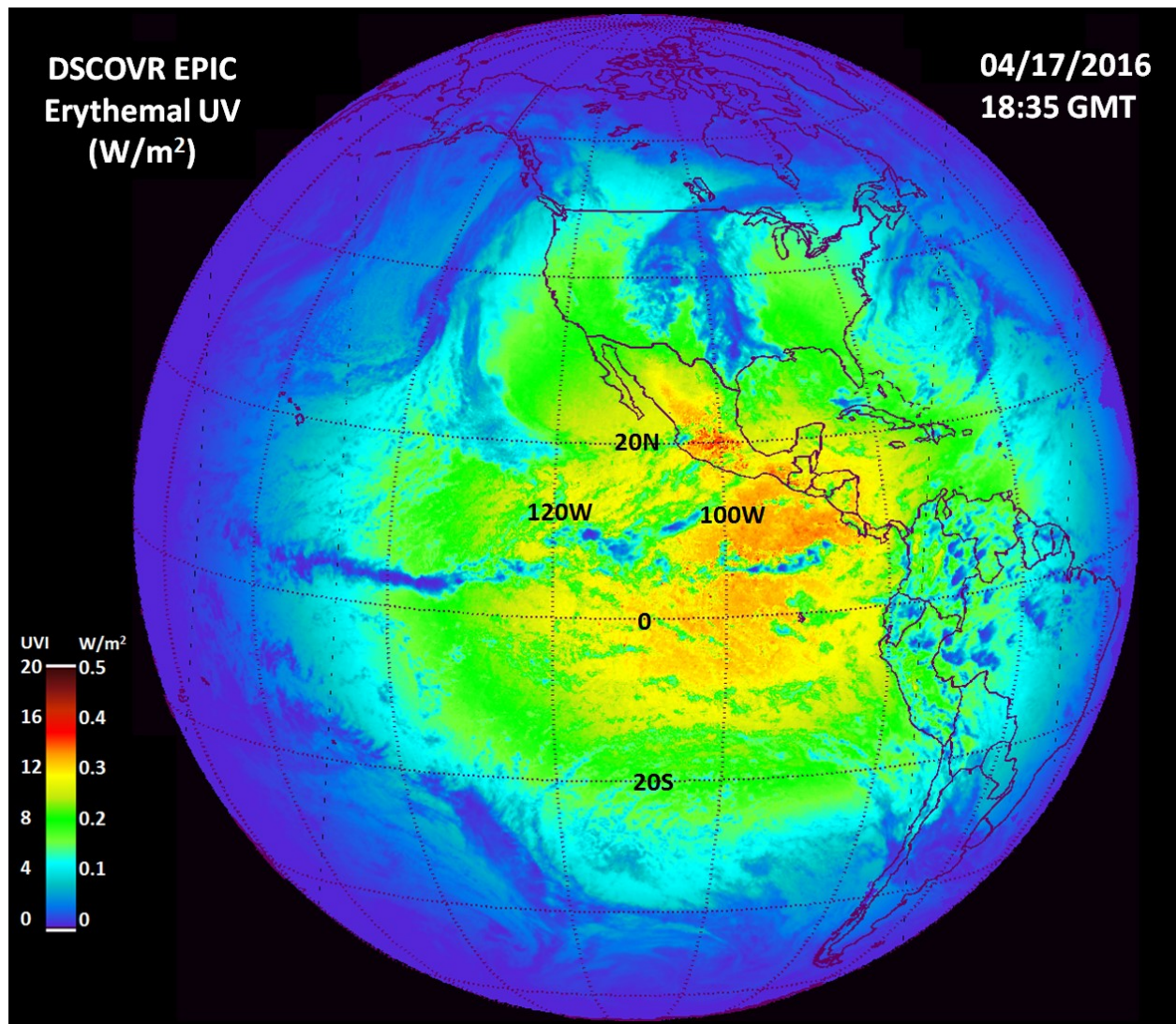
f17

759

760
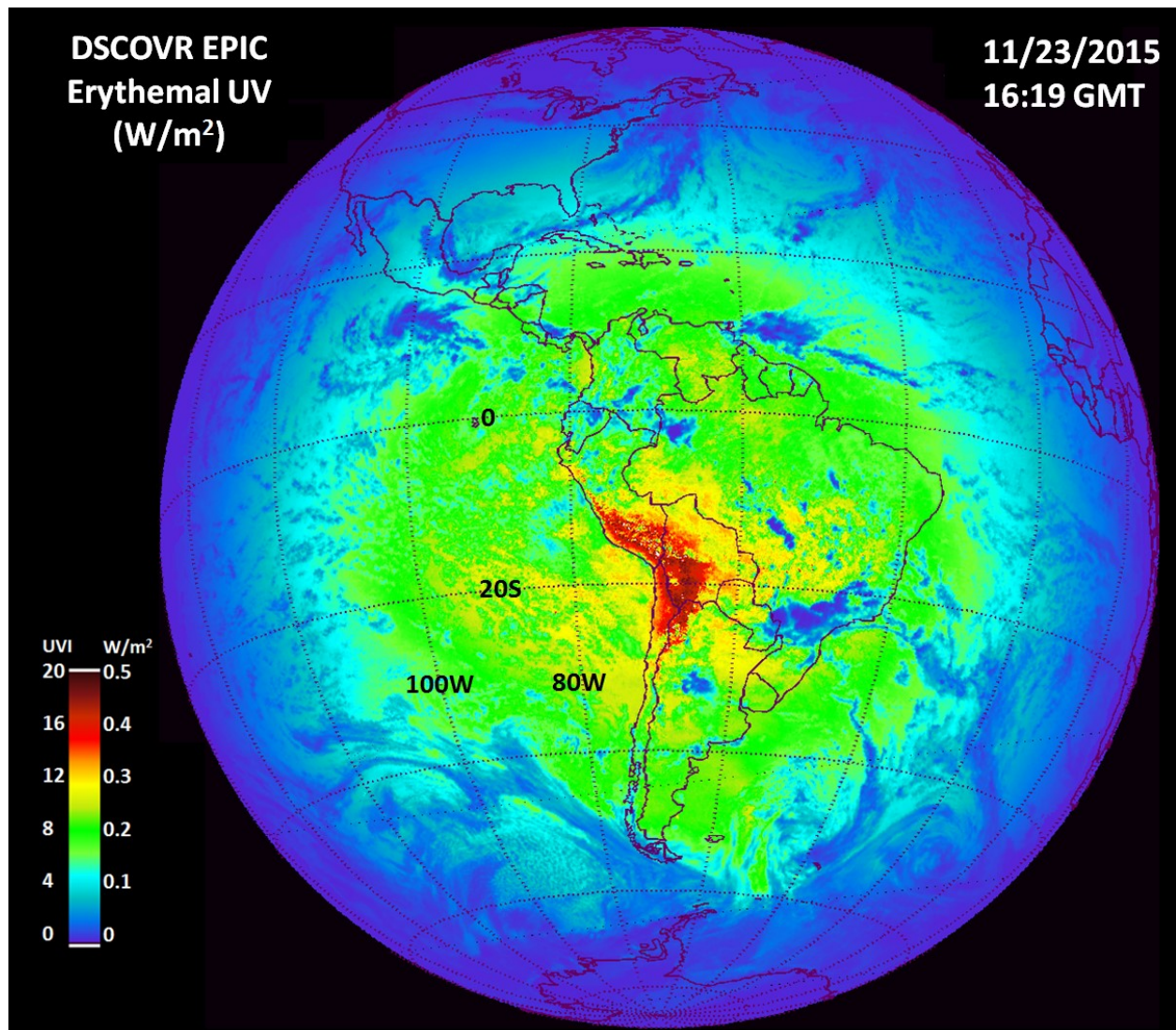
f18

761

762
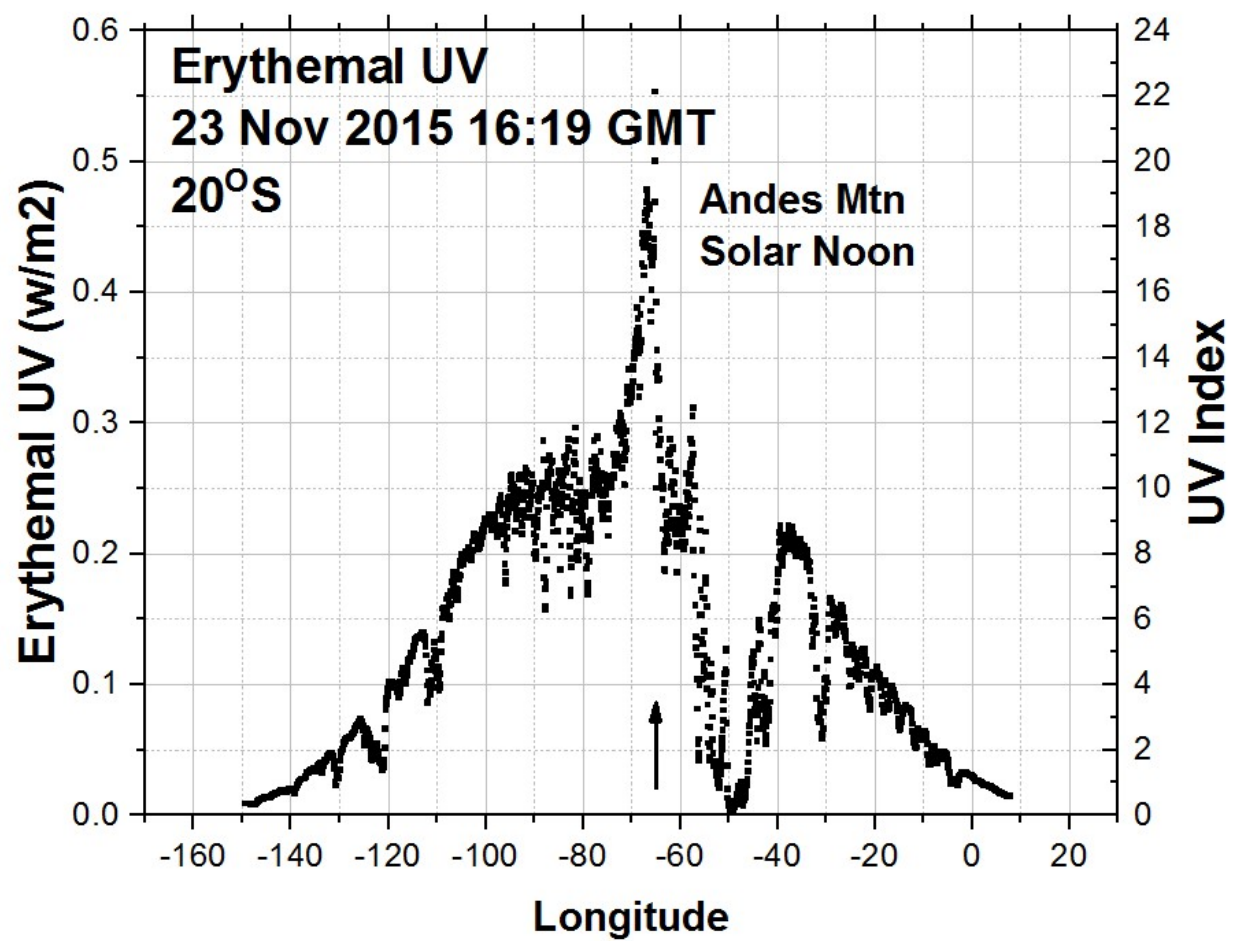
f19

764

765

f20

766

767

f21
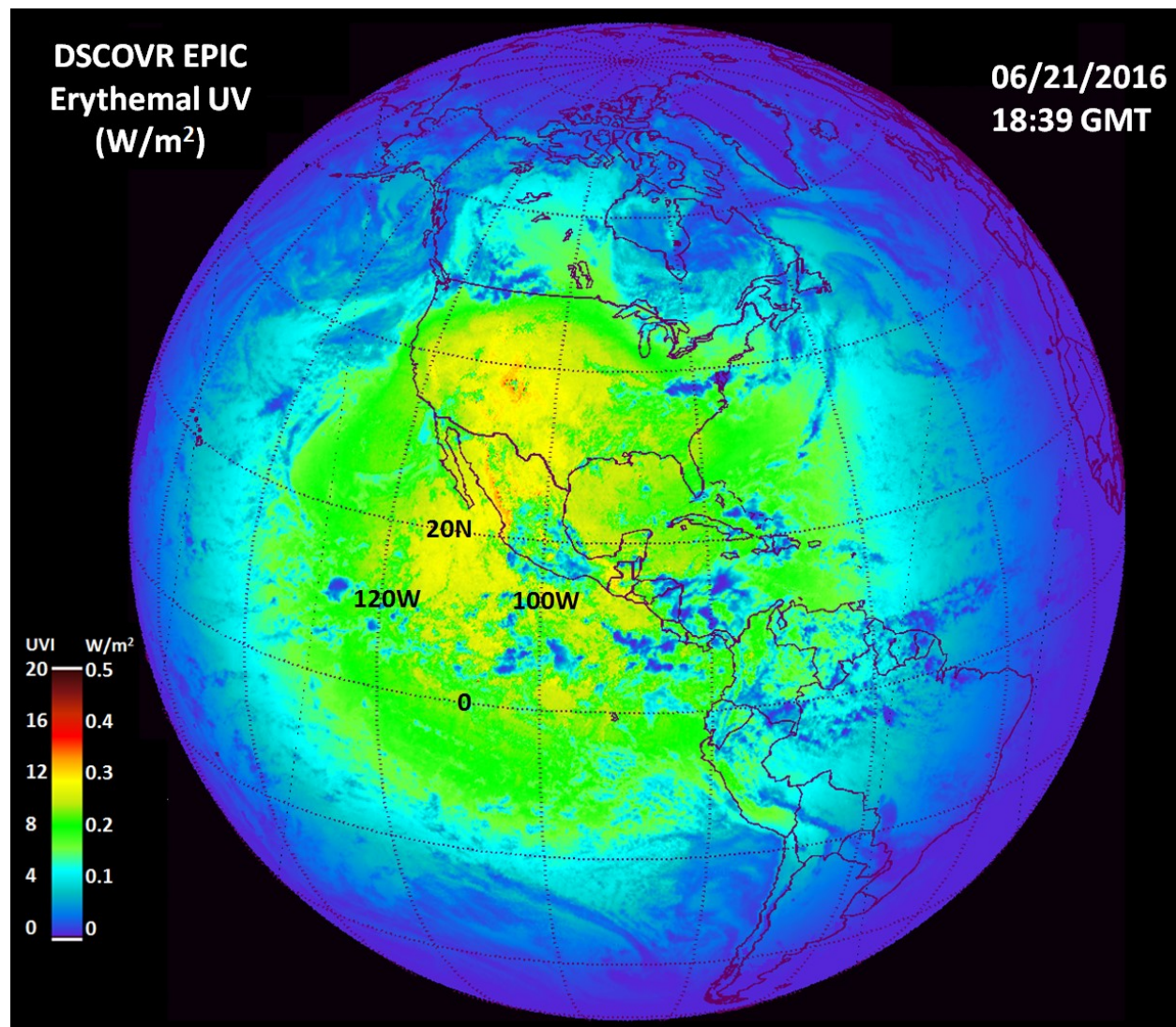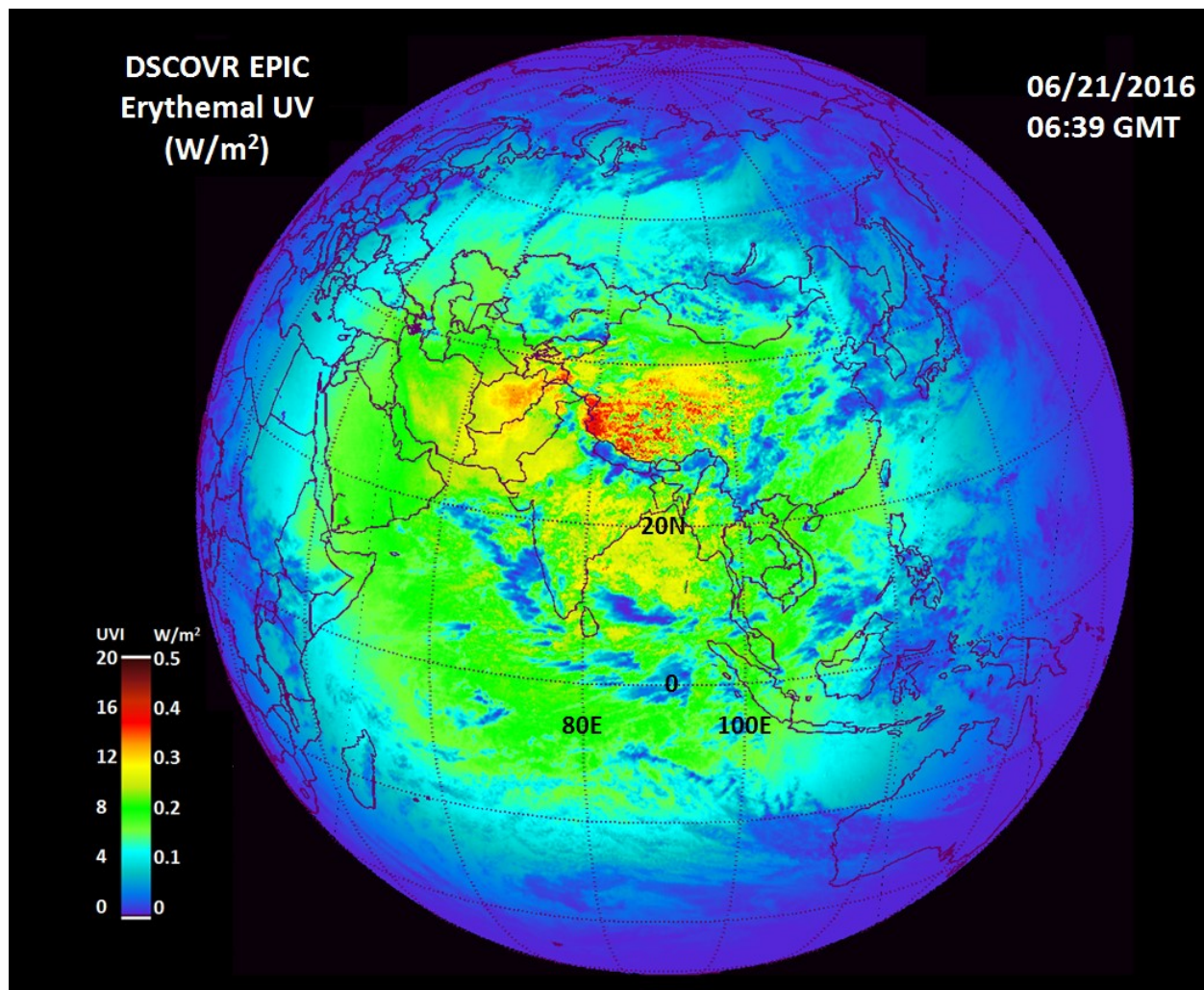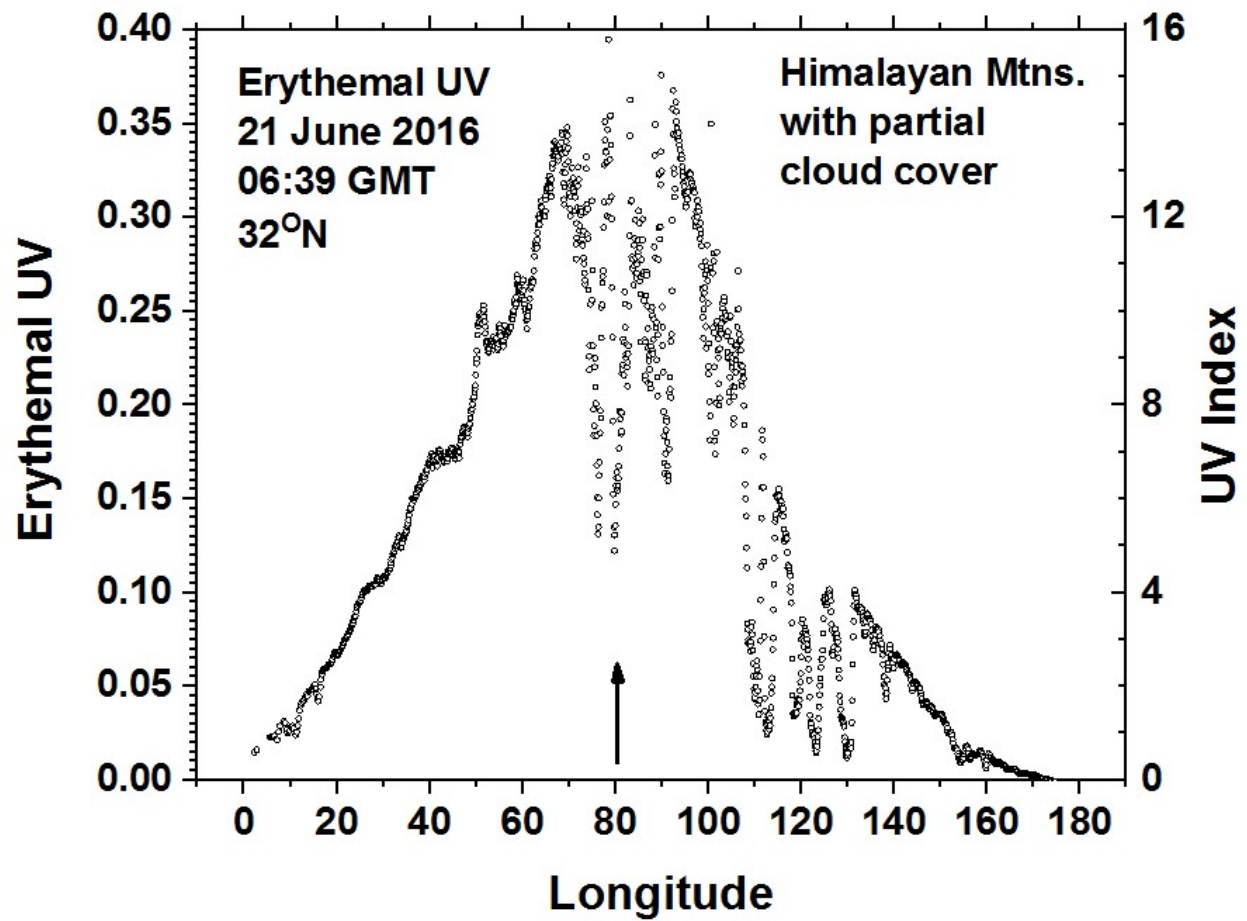
f22

770

771

772

773

774

fA1

775